


# Development of an efficient impurity solver in dynamical mean field theory for multiband systems: Iterative perturbation theory combined with parquet equations

Ryota Mizuno ,\* Masayuki Ochi, and Kazuhiko Kuroki

*Department of Physics, Osaka University, 1-1 Machikaneyama, Toyonaka, Osaka 560-0043, Japan*



(Received 26 January 2021; revised 18 July 2021; accepted 20 July 2021; published 30 July 2021)

Although several impurity solvers in the dynamical mean field theory (DMFT) have been proposed, especially in multiband systems, there are practical difficulties arising from a trade-off between numerical costs and reliability. In this study, we reinterpret the iterative perturbation theory (IPT) as an approximation which captures the strong correlation effects by mimicking the particular frequency structures of the exact full vertex, and extend it such that it can have efficiency and reliability simultaneously by modifying IPT vertex using the parquet equations. We apply this method to several models to evaluate their validity. We confirm that our method shows good agreements with the numerically exact continuous-time quantum Monte Carlo method in the single-site DMFT calculation.

DOI: [10.1103/PhysRevB.104.035160](https://doi.org/10.1103/PhysRevB.104.035160)

## I. INTRODUCTION

Strongly correlated systems exhibit many exciting phenomena such as high-temperature superconductivity, metal-insulator transition, and so on. However, these mechanisms cannot be understood in detail. These phenomena emerge in the region where both the perturbation expansions from the itinerant and localized pictures break down. In addition to this nonperturbative nature, we need to consider multiorbital or multisite degrees of freedom. Due to these complexities, these phenomena are still unresolved problems even though several decades have passed since their discovery. It is one of the central issues in condensed matter physics to understand the strong correlation effects.

Dynamical mean field theory (DMFT) [1] is one of the most powerful methods to study the strongly correlated systems. DMFT is a method in which the lattice problem is solved nonperturbatively by mapping it onto an impurity problem. DMFT can treat the temporal fluctuation correctly and can connect the itinerant and localized limits smoothly. Although DMFT has these excellent features, it cannot describe the phenomena such as anisotropic superconductivity or pseudogap since the spatial fluctuation is ignored. To resolve this problem, extensions which take into account the spatial fluctuation in DMFT were developed [2,3]. Further, formalisms to combine DMFT with *ab initio* methods were established, and so DMFT is nowadays applied to various realistic calculations.

As mentioned above, in DMFT, the lattice problem is solved by mapping it onto an impurity problem. The most widely used impurity solver is the continuous-time quantum Monte Carlo method (CT-QMC) [4–10], which is numerically exact. However, in multiband systems, it can suffer from a serious sign problem and the numerical cost necessary to

obtain results with sufficiently small statistical errors grows rapidly with increasing the number of bands. In addition, the numerical cost can also increase due to the exponential growth of the Fock space of the multiband impurity problem in the hybridization expansion of CT-QMC (CT-HYB) [4–6] and the growth of the average perturbation order in the interaction expansion (CT-INT) [8–10]. Another exact impurity solver is the exact diagonalization method (ED) [11–15]. Although the formalism of ED itself is exact, we need to discretize the electron bath in actual calculations. When we apply it to multiband systems, the discretization error can become worse because of the trade-off relation between the numbers of the impurity orbitals and bath levels. Since at least two bath levels per impurity orbital are required to obtain reliable results [13–15], the numerical cost grows exponentially with increasing the number of bands. Moreover, the broadening procedures to obtain the continuous spectrum from the resulting discrete spectrum have ambiguity. To avoid this practical difficulty, it is often necessary to use a numerically low-cost approximation method as an impurity solver. The iterative perturbation theory (IPT) [16–20], which we bring up in this paper, is one of these methods.

The original IPT was developed as a very simple approximation, in which the self-energy is calculated by the second-order perturbation. This self-energy coincidentally reproduces the atomic (strong correlation) limit in the electron-hole symmetric case. Hence, in this condition, IPT is a highly useful method which can connect the weakly and strongly correlated regime even though it is a perturbation scheme. Later, the modified-IPT, which is an extended version for an electron-hole asymmetric case, was developed [21–23]. In this method, the self-energy is parameterized so that it reproduces the exact solutions in the high-frequency and the atomic limits. By this improvement, IPT became able to be applied to the electron-hole asymmetric systems. Further improvement for multiorbital systems has been made [24–27]. Similarly to the modified-IPT, the parameters are determined such that the

\*mizuno@presto.phys.sci.osaka-u.ac.jp

self-energy reproduces the high-frequency limit. In multi-orbital systems, however, since the exact solution in the atomic limit cannot be obtained in a simple form, the self-energy is determined such that it reproduces the approximate solution in the atomic limit. Hence the scopes of the application of these methods are quite restricted.

As described above, IPT has been regarded as a method which interpolates the weak and strong correlation limits. In this study, we provide IPT with a new interpretation in which IPT captures the strong correlation effects by mimicking the particular frequency structures of the exact full vertex, and extend the method such that it can be applied to multiband systems. We validate this method by applying it to several models and comparing with the numerically exact CT-QMC method.

This paper is organized as follows. In Sec. II, we define the models and outline the Green's function method. We describe in Sec. III the novel method developed in the present study. Results are shown in Sec. IV. The discussion is presented in Sec. V. The conclusion is given in Sec. VI.

## II. MODEL AND GREEN FUNCTION

### A. Definitions

We consider the Hubbard model for multiband systems described by the following Hamiltonian:

$$H = \sum_{ij} \sum_{\alpha\beta} t_{ij,\alpha\beta} c_{i\alpha}^\dagger c_{j\beta} + \frac{1}{4} \sum_i \sum_{\alpha\beta\gamma\lambda} U_{\alpha\beta\gamma\lambda} c_{i\alpha}^\dagger c_{i\lambda}^\dagger c_{i\gamma} c_{i\beta}, \quad (1)$$

where the subscripts with Roman letters indicate unit cells and Greek letters the set of the degree of freedom of spin, orbital, and site.  $t_{ij,\alpha\beta}$  is the hopping integral and  $U_{\alpha\beta\gamma\lambda}$  is the Coulomb repulsion.  $c_{i\alpha}^{(\dagger)}$  is the annihilation (creation) operator.

The  $n$ -particle Green's function is defined as

$$G_{i_1, \dots, i_{2n}, \alpha_1, \dots, \alpha_{2n}}^{(n)}(\tau_1, \dots, \tau_{2n}) = (-1)^n \langle T [c_{i_1 \alpha_1}(\tau_1) c_{i_2 \alpha_2}^\dagger(\tau_2) \cdots c_{i_{2n-1} \alpha_{2n-1}}(\tau_{2n-1}) c_{i_{2n} \alpha_{2n}}^\dagger(\tau_{2n})] \rangle, \quad (2)$$

where  $c^{(\dagger)}(\tau) = e^{\tau H} c^{(\dagger)} e^{-\tau H}$  is the Heisenberg representation of annihilation (creation) operators.  $\langle A \rangle = \text{Tr}(e^{-\beta H} A) / Z$  is the statistical average of  $A$  and  $Z = \text{Tr}(e^{-\beta H})$  is the partition function.

In the presence of the time and lattice translational invariance, the one-particle Green's function [ $n = 1$  in Eq. (2)] in the momentum space can be written as

$$G_{\alpha\beta}(\mathbf{k}, \tau) \equiv G_{\alpha\beta}^{(1)}(\mathbf{k}, \tau) = -\langle T c_{k\alpha}(\tau) c_{k\beta}^\dagger \rangle, \quad (3)$$

where  $\mathbf{k}$  denotes the momentum. The Fourier transformation in terms of the imaginary time is expressed as

$$G_{\alpha\beta}(\mathbf{k}, \tau) = \frac{1}{\beta} \sum_n G_{\alpha\beta}(\mathbf{k}, i\omega_n) e^{-i\omega_n \tau}, \quad (4)$$

$$G_{\alpha\beta}(\mathbf{k}, i\omega_n) = \int d\tau G_{\alpha\beta}(\mathbf{k}, \tau) e^{i\omega_n \tau}, \quad (5)$$

where  $\omega_n = (2n+1)\pi T$  with  $n \in \mathbb{Z}$  is a fermionic Matsubara frequency ( $\nu_m = 2m\pi T$  introduced later is a bosonic Mat-

subara frequency).  $G(\mathbf{k}, i\omega_n)$  can be derived in the following form:

$$\hat{G}(k) = [(i\omega_n + \mu)\hat{I} - \hat{\epsilon}_k - \hat{\Sigma}(k)]^{-1}, \quad (6)$$

where  $\mu$  is the chemical potential and  $k = (\mathbf{k}, i\omega_n)$  is the generalized fermionic momentum [ $q = (\mathbf{q}, i\nu_m)$  introduced later denotes the generalized bosonic momentum].  $\hat{\epsilon}_k = N_k^{-2} \sum_{ij} \hat{t}_{ij} e^{i(\mathbf{R}_i - \mathbf{R}_j) \cdot \mathbf{k}}$  is the band dispersion and  $\hat{\Sigma}(k)$  is the self-energy. These quantities are matrices in terms of the band index and  $\hat{I}$  is the unit matrix.

Similarly to the one-particle case, in the presence of the time and lattice translational invariance, the two-particle Green's function [ $n = 2$  in Eq. (2)] in the momentum space can be written as

$$G_{\alpha\beta\gamma\lambda}^{(2)}(\mathbf{k}, \mathbf{k}', \mathbf{q}, \tau_1, \tau_2, \tau_3) = \langle T c_{k\alpha}(\tau_1) c_{k+q\beta}^\dagger(\tau_2) c_{k'+q\lambda}(\tau_3) c_{k'\gamma}^\dagger \rangle. \quad (7)$$

Fourier transformation is given by

$$\hat{G}^{(2)}(\mathbf{k}, \mathbf{k}', \mathbf{q}, \tau_1, \tau_2, \tau_3) = \frac{1}{\beta^3} \sum_{nn'm} \hat{G}^{(2)}(\mathbf{k}, \mathbf{k}', \mathbf{q}, i\omega_n, i\omega_{n'}, i\nu_m) \times e^{-i\omega_n \tau_1} e^{i(\omega_n + \nu_m) \tau_2} e^{-i(\omega_{n'} + \nu_m) \tau_3}. \quad (8)$$

The two-particle Green's function can be divided into two parts: disconnected and connected terms

$$G_{\alpha\beta\gamma\lambda}^{(2)}(k, k', q) = G_{\alpha\beta}(k) G_{\lambda\gamma}(k') \delta_{q,0} - G_{\alpha\gamma}(k) G_{\lambda\beta}(k+q) \delta_{kk'} + \sum_{\alpha'\beta'\gamma'\lambda'} G_{\alpha\gamma'}(k) G_{\lambda'\beta}(k+q) F_{\gamma'\lambda'\alpha'\beta'} \times (k, k', q) G_{\alpha'\gamma'}(k') G_{\lambda\beta'}(k'+q), \quad (9)$$

where  $\hat{F}$  is called the full vertex. Introducing the irreducible susceptibility

$$\chi_{0,\alpha\beta\gamma\lambda}(k, k', q) = -G_{\alpha\gamma}(k) G_{\lambda\beta}(k+q) \delta_{kk'}, \quad (10)$$

we can define the generalized susceptibility as

$$\hat{\chi}_G(k, k', q) = \hat{\chi}_0(k, k', q) - \hat{\chi}_0(k, q) \hat{F}(k, k', q) \hat{\chi}_0(k', q). \quad (11)$$

Also we can write the self-energy by using full vertex as

$$\Sigma_{\alpha\beta}(k) = \Sigma_{\alpha\beta}^{\text{HF}} + \frac{1}{2} \sum_{\gamma\lambda} \sum_{k',q} [\hat{F}(k, k', q) \hat{\chi}_0(k', q) \hat{U}]_{\alpha\gamma\beta\lambda} \times G_{\gamma\lambda}(k+q), \quad (12)$$

where  $\Sigma^{\text{HF}}$  is the Hartree-Fock term.

### B. Parquet formalism

To consider the diagrammatic structure of the full vertex  $F$ , we have to define the irreducible susceptibilities concerning the following three channels (ph,  $\overline{\text{ph}}$ , pp):

$$\chi_{0,\alpha\beta\gamma\lambda}(k, k', q) = \begin{cases} -G_{\alpha\gamma}(k) G_{\lambda\beta}(k+q) \delta_{kk'} & (\text{ph}), \\ G_{\alpha\beta}(k) G_{\lambda\gamma}(k') \delta_{q0} & (\overline{\text{ph}}), \\ G_{\alpha\gamma}(k) G_{\beta\lambda}(-k-q) \delta_{kk'} & (\text{pp}), \end{cases} \quad (13)$$

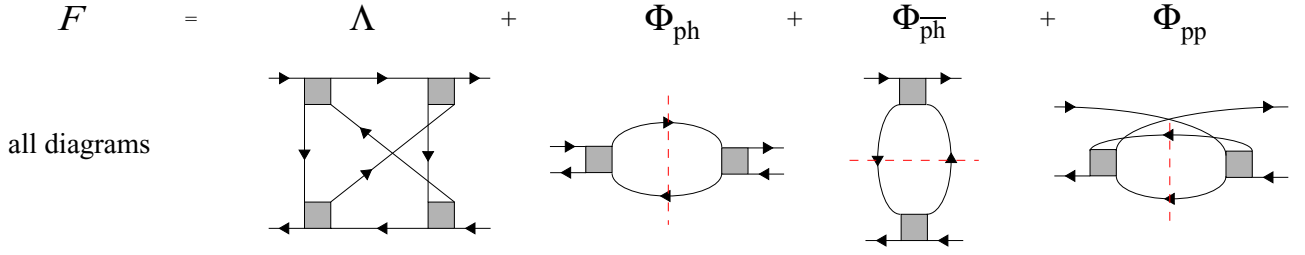


FIG. 1. The decomposition of the full vertex. The full vertex can be divided into four parts: the fully irreducible part ( $\Lambda$ ) and the reducible parts ( $\Phi_l, l = \text{ph}, \overline{\text{ph}}, \text{pp}$ ).

The ph channel in Eq. (13) is the same as Eq. (10). The full vertex  $\hat{F}$  can be divided into four parts:

$$\hat{F} = \hat{\Lambda} + \hat{\Phi}_{\text{ph}} + \hat{\Phi}_{\overline{\text{ph}}} + \hat{\Phi}_{\text{pp}}, \quad (14)$$

where  $\hat{\Phi}_l$  ( $l = \text{ph}, \overline{\text{ph}}, \text{pp}$ ) is the set of reducible diagrams in channel  $l$ , and  $\hat{\Lambda}$  is the set of fully irreducible diagrams. The diagrammatic representation is shown in Fig. 1. Since there is no diagram which simultaneously satisfies reducibility in two or more channels, we can write

$$\hat{F} = \hat{\Gamma}_l + \hat{\Phi}_l, \quad (15)$$

$$\hat{\Gamma}_l = \hat{\Lambda} + \hat{\Phi}_{l_1} + \hat{\Phi}_{l_2} \quad (l \neq l_1 \neq l_2), \quad (16)$$

$$\hat{\Phi}_l = -\hat{\Gamma}_l \hat{\chi}_0 \hat{F} = -\hat{\Gamma}_l \hat{\chi}_l \hat{\Gamma}_l, \quad (17)$$

where  $\hat{\Gamma}_l$  is the set of diagrams irreducible in channel  $l$  and is called the irreducible vertex in  $l$ .  $\hat{\chi}_l$  are given by

$$\hat{\chi}_l = \hat{\chi}_0 - \hat{\chi}_0 \hat{\Gamma}_l \hat{\chi}_l = \hat{\chi}_0 - \hat{\chi}_0 \hat{F} \hat{\chi}_0. \quad (18)$$

From Eqs. (15) to (18), which are called the parquet equations [28–31], we can calculate  $\hat{F}$  exactly if we know the exact  $\hat{\Lambda}$ . However, it is very difficult to obtain the exact  $\hat{\Lambda}$  and the procedure to obtain  $\hat{\Phi}_l$  is numerically very expensive. Thus, some approximations or simplifications have been proposed [32–34] (see Appendix D).

### III. NOVEL IMPURITY SOLVER: IPT + PARQUET

In this section, we develop a novel impurity solver by reinterpreting and extending IPT. First, in Sec. III A, we introduce our extension of IPT. After that in Sec. III B, we explain our new interpretation of IPT, which is the basis of the extension. Other theoretical details are in Sec. III C.

#### A. Extension of IPT

In IPT, the correlation part of the self-energy is approximated as

$$\hat{\Sigma}_{\text{IPT}}(\omega_n) = [\hat{I} - \hat{B} \hat{\Sigma}^{2\text{nd}}(i\omega_n)]^{-1} \hat{A} \hat{\Sigma}^{2\text{nd}}(i\omega_n), \quad (19)$$

$$\hat{\Sigma}_{\alpha\beta}^{2\text{nd}} = T^2 \sum_{\gamma\lambda} \sum_{\omega_n' \nu_m} [\hat{U} \hat{\chi}_0(\omega_n', \nu_m) \hat{U}]_{\alpha\gamma\beta\lambda} G_{0,\gamma\lambda}(\omega_n + \nu_m), \quad (20)$$

$$\chi_{0,\alpha\beta\gamma\lambda}(\omega_n, \nu_m) = -G_{0,\alpha\gamma}(\omega_n) G_{0,\lambda\beta}(\omega_n + \nu_m), \quad (21)$$

$$\hat{G}_0(i\omega_n) = [(i\omega_n + \mu_0) \hat{I} - \hat{\Delta}(i\omega_n) - \hat{\Sigma}^{\text{HF}}]^{-1}, \quad (22)$$

where  $\mu_0$ ,  $\hat{\Delta}(i\omega)$ , and  $\hat{\Sigma}^{\text{HF}}$  are the pseudochemical potential, the hybridization function, and the Hartree-Fock term in the self-energy, respectively. The parameters  $\hat{A}$ ,  $\hat{B}$  are determined such that one reproduces the exact solutions in the high frequency and atomic limits:

$$\hat{A} = \frac{n(1-n)}{n_0(1-n_0)} \hat{I}, \quad \hat{B} = \frac{(1-2n)U + \mu_0 - \mu}{n_0(1-n_0)U^2} \hat{I}, \quad (23)$$

where  $n_0$  and  $n$  are the electron numbers evaluated from  $\hat{G}_0(i\omega_n)$  and  $\hat{G}(i\omega_n)$ , respectively. Although this is the IPT formalism for the single-band systems, we intentionally write it in the matrix form for the extension below.

We extend the IPT as follows:

$$\hat{\Sigma}_{\text{IPT+parquet}}^{\text{CR}}(\omega_n) = [\hat{I} - \hat{B} \hat{\Sigma}_0^{\text{CR}}(\omega_n)]^{-1} \hat{A} \hat{\Sigma}_0^{\text{CR}}(\omega_n), \quad (24)$$

$$\begin{aligned} \Sigma_{0,\alpha\beta}^{\text{CR}}(\omega_n) &= T^2 \sum_{\gamma\lambda} \sum_{\omega_n' \nu_m} [\hat{F}_0(\omega_n, \omega_n', \nu_m) \hat{\chi}_0(\omega_n', \nu_m) \hat{U}]_{\alpha\gamma\beta\lambda} \\ &\times G_{0,\gamma\lambda}(\omega_n + \nu_m), \end{aligned} \quad (25)$$

$$\chi_{0,\alpha\beta\gamma\lambda}(\omega_n, \nu_m) = -G_{0,\alpha\gamma}(\omega_n) G_{0,\lambda\beta}(\omega_n + \nu_m), \quad (26)$$

$$\hat{G}_0(\omega_n) = [i\omega_n \hat{I} + \hat{\mu}_0 - \hat{\Delta}(\omega_n) - \hat{\Sigma}^{\text{HF}}]^{-1}, \quad (27)$$

$$\begin{aligned} \hat{F}_0(\omega_n, \omega_n', \nu_m) &= \hat{U} + \hat{\Phi}_{\text{ph}}(\nu_m) + \hat{\Phi}_{\overline{\text{ph}}}(\omega_n - \omega_n') \\ &+ \hat{\Phi}_{\text{pp}}(\omega_n + \omega_n' + \nu_m), \end{aligned} \quad (28)$$

where  $\hat{F}_0$  is an approximate full vertex. To obtain  $\hat{F}_0$ , we employ the simplified parquet method developed in Ref. [32]. (We explain the reason why we employ the simplified parquet method in Sec. III B). Hence, we call this ‘‘IPT + parquet method.’’ Since the simplified parquet method in Ref. [32] supports only the single-band calculations, we extend it for the multiband calculations and its detailed procedure to obtain  $\hat{F}_0$  is shown in Appendix D. In practical calculation, however, we omit the contribution from pp channel  $\hat{\Phi}_{\text{pp}}$  when calculating the self-energy in Eq. (27) since  $\hat{\Phi}_{\text{pp}}$  tends to be overestimated. We add a band index to the pseudochemical potential  $\mu_0$  in Eq. (22), and so  $\hat{\mu}_0$  in Eq. (27) is a diagonal matrix. The reason for this modification and the conditions for the parameters  $\hat{A}$ ,  $\hat{B}$ , and  $\hat{\mu}_0$  are discussed later in Sec. III C.

This extension is based on the interpretation in which IPT captures the strong correlation effects by mimicking the particular frequency structures of the exact full vertex.

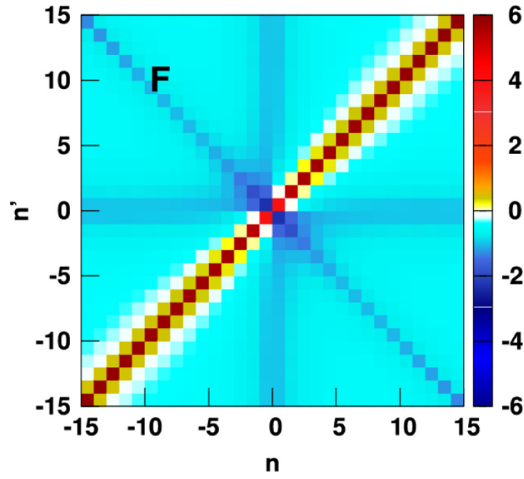


FIG. 2. The frequency dependence of the full vertex in the charge channel obtained in QMC as an impurity solver. The bare interaction  $U$  is subtracted. The calculations were performed for the Hubbard model on a square lattice with nearest-neighbor hopping  $t$  at  $T/t = 0.4$ ,  $U/t = 5.08$ . The intensity is given in units of  $4t$ . This figure is taken from Ref. [3].

We explain this new interpretation in detail in the next section.

### B. Reinterpretation of IPT

To present our new interpretation of IPT, we explain the frequency structure of the exact full vertex [3,29,35]. Figure 2 shows the full vertex in the charge channel  $F^c(i\omega_n, i\omega_{n'}, i\nu_m)$  in the  $n$ - $n'$  plane calculated with the QMC as the impurity solver [3,35]. As we can see from this figure,  $F^c(i\omega_n, i\omega_{n'}, i\nu_m)$  takes large values in the vicinity of the diagonal line in the  $n$ - $n'$  plane.  $\overline{\text{ph}}$  and  $\text{pp}$  channels exhibit large values in the vicinity of  $\omega_n - \omega_{n'} = 0$  and  $\omega_n + \omega_{n'} + \nu_m = 0$ , respectively. These large values on the diagonal lines come from these channels. The  $\text{ph}$  channel takes large values near  $\nu_m = 0$  although it is not depicted in Fig. 2. This structure coming from  $\overline{\text{ph}}$ ,  $\overline{\text{ph}}$ , and  $\text{pp}$  channels is called the “diagonal structure” [36–39]. We can also see that  $F^c(i\omega_n, i\omega_{n'}, i\nu_m)$  takes large values in the vicinity of  $\omega_n = 0$  and  $\omega_{n'} = 0$  lines. This cross-shaped structure is called the “cross structure” [36–39]. There is one more characteristic structure which  $F^c(i\omega_n, i\omega_{n'}, i\nu_m)$  depends on  $\omega_n$  and  $\omega_{n'}$  independently and has large values near the center of the  $n$ - $n'$  plane. We call this the “central structure.” The contribution from the cross and central structures is important in the strongly correlated regime since these two structures come from the higher-order diagrams than that of the diagonal structure (see Appendix B for details).

Given this, we move on to IPT. Comparing Eq. (19) with the exact expression of the correlation part of the self-energy  $\hat{\Sigma}^{\text{CR}}(i\omega_n)$  using the full vertex

$$\Sigma_{\alpha\beta}^{\text{CR}}(\omega_n) = T^2 \sum_{\gamma\lambda} \sum_{\omega_n', \nu_m} [\hat{F}(\omega_n, \omega_{n'}, \nu_m) \hat{\chi}_0(\omega_{n'}, \nu_m) \hat{U}]_{\alpha\gamma\beta\lambda} \times G_{\gamma\lambda}(\omega_n + \nu_m), \quad (29)$$

$$\chi_{0,\alpha\beta\gamma\lambda}(\omega_n, \nu_m) = -G_{\alpha\gamma}(\omega_n) G_{\lambda\beta}(\omega_n + \nu_m), \quad (30)$$

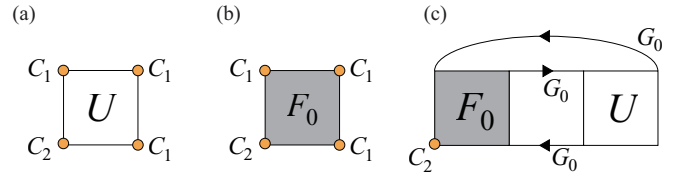


FIG. 3. Diagrammatic representation of (a) the full vertex of IPT, (b) the full vertex of IPT + parquet, and (c) the self-energy.

the full vertex in IPT can be written as

$$[F_{\text{IPT}}(\omega_n, \omega_{n'}, \nu_m)]_{\alpha\beta\gamma\lambda} = C_{2,\alpha\alpha'}(\omega_n) C_{1,\beta\beta'}(\omega_n + \nu_m) \times U_{\alpha'\beta'\gamma'\lambda'} C_{1,\gamma'\gamma}(\omega_{n'}) C_{1,\lambda'\lambda}(\omega_{n'} + \nu_m), \quad (31)$$

$$\hat{C}_1(\omega_n) = \hat{G}_0(\omega_n) \hat{G}^{-1}(\omega_n), \quad (32)$$

$$\hat{C}_2(\omega_n) = [\hat{I} - \hat{B} \hat{\Sigma}^{(2)}(\omega_n)]^{-1} \hat{A}. \quad (33)$$

The diagrammatic representation of  $\hat{F}_{\text{IPT}}$  is shown in Fig. 3(a). Figures 4(a) and 4(b) show the full vertex in the atomic limit  $\hat{F}_{\text{atom}}$  [29] subtracted by the terms which give the diagonal structure ( $\overline{\text{ph}}$ ,  $\overline{\text{ph}}$ ,  $\text{pp}$  terms) and constant  $\hat{U}$ , and Figs. 4(c) and 4(d) show  $\hat{F}_{\text{IPT}}$  in a single-band case. We can see that these structures resemble each other and hence we can say that the IPT is an approximation which captures the strong correlation effects by the “pseudo”cross and central structures. On the other hand, IPT fails to capture the diagonal structure as we

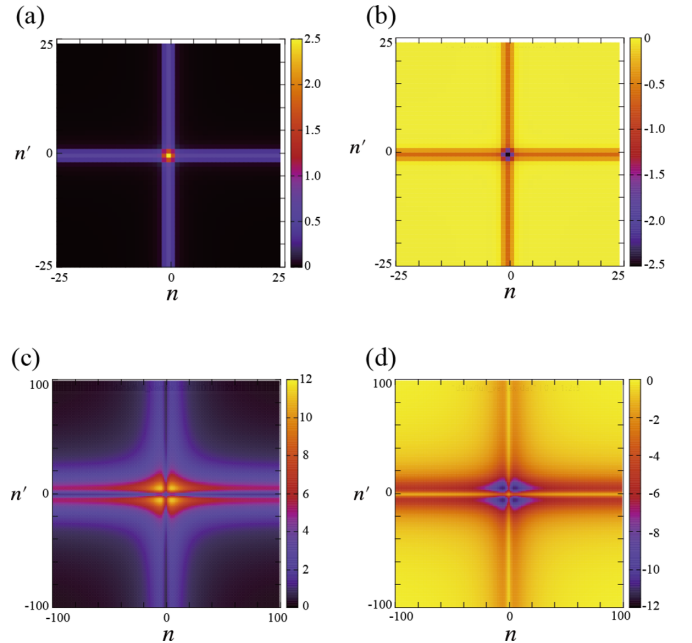


FIG. 4. The frequency dependence of the full vertex at  $\nu_m = 0$ . Upper panels: The frequency dependence of the full vertex in the atomic limit subtracted by the bare interaction and the terms that give the diagonal structure ( $\overline{\text{ph}}$ ,  $\overline{\text{ph}}$ ,  $\text{pp}$  term). Lower panels: The frequency dependence of the full vertex in IPT. (a,c) correspond to the charge channel, and (b,d) the spin channel.



can see from Eq. (31), where the  $\omega_n - \omega_{n'}$  and  $\omega_n + \omega_{n'} + \nu_m$  dependencies are absent.

This is a new interpretation of IPT and is completely different from the conventional one in which IPT is considered as an interpolation method from the weak and strong correlation limits. It should be noted that correctly reproducing the frequency dependence of one-body quantities (e.g., self-energy) does not necessarily imply reproducing that of two-body quantities. Therefore, we believe it is more appropriate to recognize that IPT correctly captures the strong correlation effects because it mimics the cross and central structures of the full vertex, not simply because it reproduces the exact solution of the self energy in the strong correlation limit.

This reinterpretation naturally leads to the extension of IPT in Sec. III A. As mentioned above, IPT fails to capture the diagonal structure of the full vertex. This structure can be captured by the following replacement:

$$\begin{aligned} [F_{\text{IPT}}(\omega_n, \omega_{n'}, \nu_m)]_{\alpha\beta\gamma\lambda} & \\ &= C_{2,\alpha\alpha'}(\omega_n)C_{1,\beta\beta'}(\omega_n + \nu_m) \\ &\quad \times U_{\alpha'\beta'\gamma'\lambda'}C_{1,\gamma'\gamma'}(\omega_{n'})C_{1,\lambda'\lambda}(\omega_{n'} + \nu_m), \end{aligned} \quad (34)$$

↓

$$\begin{aligned} [F_{\text{IPT+parquet}}(\omega_n, \omega_{n'}, \nu_m)]_{\alpha\beta\gamma\lambda} & \\ &= C_{2,\alpha\alpha'}(\omega_n)C_{1,\beta\beta'}(\omega_n + \nu_m) \\ &\quad \times F_{0,\alpha'\beta'\gamma'\lambda'}(\omega_n, \omega_{n'}, \nu_m)C_{1,\gamma'\gamma'}(\omega_{n'})C_{1,\lambda'\lambda}(\omega_{n'} + \nu_m), \end{aligned} \quad (35)$$

where  $\hat{C}_2$  in Eq. (33) is also replaced with

$$\hat{C}_2(\omega_n) = [\hat{I} - \hat{B}\hat{\Sigma}_0^{\text{CR}}(\omega_n)]^{-1}\hat{A}. \quad (36)$$

The diagrammatic representation of the self-energy and full vertices are shown in Fig. 3. Substituting the full vertex in Eq. (35) into the exact expression of the self-energy in Eq. (29), we obtain Eqs. (24) to (28). As mentioned in Sec. III A, we employ the simplified parquet method developed in Ref. [32] to obtain  $\hat{F}_0$ . The approximate full vertex  $\hat{F}_0$  needs to (i) have only diagonal and constant terms because the cross and central terms are given by  $C_1$ , and (ii) be obtained with low numerical cost so as not to lose the advantage of IPT. The simplified parquet method can meet these requirements because it can provide the diagonal and constant terms with low numerical cost while ignoring the cross and central structures (see Appendix D).

While we employ simplified parquet method here,  $\hat{F}_0$  can be evaluated by other methods as long as they estimate only the diagonal and constant parts of the full vertex. Indeed, in Sec. IV A, we show the result of ‘‘IPT + FLEX’’ in which we obtain  $\hat{F}_0$  in Eq. (28) by the fluctuation exchange (FLEX) approximation [40] for comparison. On the other hand, for example, the exact full vertex of the atomic limit  $\hat{F}_{\text{atom}}$  or the full vertex obtained from the nonsimplified parquet method are not suitable for  $\hat{F}_0$  since they already have the cross and central structures and hence yield double counting if adopted.

Finally, we should note that the ansatz in Eqs. (32), (33), and (36) (more generally the choice of  $\hat{C}_1 \neq \hat{C}_2$ ) breaks the crossing symmetry of the full vertex. In fact, in a separate publication Ref. [41], we developed a method in which we

defined a different full vertex that reproduced the same self-energy without breaking the crossing symmetry.

### C. How to determine the parameters $A$ , $B$ , and $\mu_0$

The remaining problem here is how to deal with the parameters  $\hat{A}$ ,  $\hat{B}$  in Eq. (24), and  $\hat{\mu}_0$  in Eq. (27) in the multiband systems. In MO-IPT [26,27], the two or more particle effects are added in the form of the static correlation functions when the single-orbital IPT is extended to the multiorbital one. By contrast, in our formalism, these effects are already considered in the form of the diagonal terms of the dynamical full vertex obtained by the parquet equations. Therefore, we simply extend the single-orbital representation of parameters Eq. (23) to multiorbital forms, as follows:

$$A_{\alpha\beta} = \delta_{\alpha\beta}, \quad (37)$$

$$B_{\alpha\beta} = \delta_{\alpha\beta} \frac{N_{\text{orbital}}^{-1} \sum_{\gamma} U_{\alpha\alpha\gamma\gamma}(1 - 2n_{\gamma}) + \mu_{0\alpha\alpha} - \mu}{\sum_{\gamma} U_{\alpha\alpha\gamma\gamma}n_{0\gamma}(1 - n_{0\gamma})U_{\gamma\gamma\alpha\alpha}}, \quad (38)$$

where  $n_{\alpha}$ ,  $n_{0\alpha}$  is the band filling evaluated from  $\hat{G}$ ,  $\hat{G}_0$ . In addition, we add a degree of freedom to the pseudochemical potential as  $\mu_0 \rightarrow \hat{\mu}_0$  (i.e., not a scalar but a diagonal matrix) to satisfy the condition  $n_{\alpha} = n_{0\alpha}$ , and so  $\hat{A}$  is fixed to unity. This condition is needed for the following reason. According to the interpretation introduced in Sec. III B, the correction factor  $\hat{C}_1 = \hat{G}_0\hat{G}^{-1}$  captures the strong correlation effects. Hence,  $\hat{C}_1$  needs to increase in the appropriate regions of filling, namely, in the vicinity of half filling. In the multiband case, if the pseudochemical potential is a single scalar parameter  $\mu_0$  (i.e., independent of the band index  $\alpha$ ),  $n_{0\alpha}$  can be different from  $n_{\alpha}$  in general even if  $\sum_{\alpha} n_{0\alpha} = \sum_{\alpha} n_{\alpha}$  is satisfied. For example, it is possible that  $n_{0\alpha}$  is at half filling but  $n_{\alpha}$  is away from it or vice versa.  $C_1$  is not appropriately given under these circumstances. Therefore, we need to regard the pseudochemical potential as a diagonal matrix  $\hat{\mu}_0$  by adding the band index  $\alpha$  to  $\mu_0$  for the condition  $n_{\alpha} = n_{0\alpha}$ .

Also, we should note that the first term in the numerator in Eq. (38) is divided by only the number of orbitals  $N_{\text{orbital}}$  (i.e., not by the number of sites  $N_{\text{site}}$ ). This is because we assume the interaction which does not have site-off-diagonal elements but has the orbital-off-diagonal elements that is comparable with the diagonal elements in magnitude. This interaction is valid in many realistic systems. The parameter  $\hat{B}$  is related to the electron-hole asymmetry (see Appendix E for details). If we take the summation over orbital index without  $N_{\text{orbital}}^{-1}$ ,  $\hat{B}$  is overestimated and then the electron-hole asymmetry is overestimated. On the other hand, if we divide the first term in the numerator in Eq. (38) by  $N_{\text{site}}$ ,  $\hat{B}$  is underestimated since the summation over the site-off-diagonal elements is zero. When we consider the interaction which has the site-off-diagonal elements or does not have the orbital-off-diagonal elements, the expression of  $\hat{B}$  in Eq. (38) has to be modified.

## IV. RESULTS

In this section, we show the results of IPT + parquet method. We use the quasiparticle weight as a probe of the

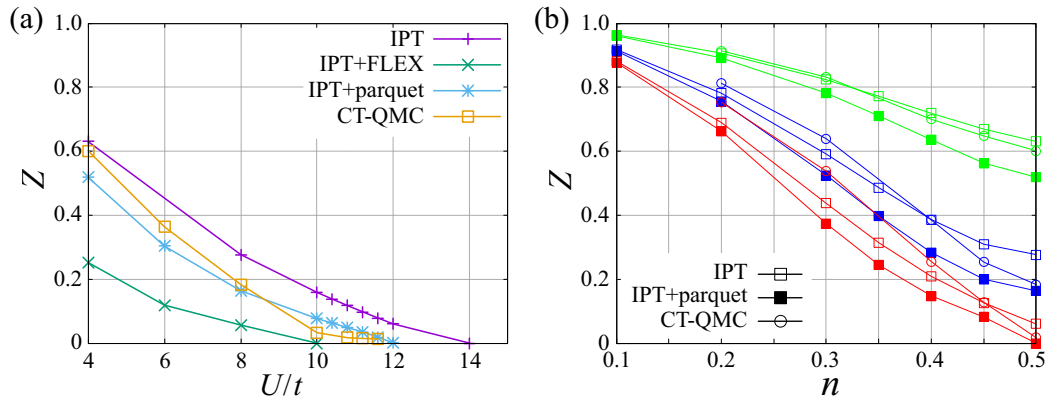


FIG. 5. Comparison of quasiparticle weight among methods. (a) The violet, blue, green, and yellow lines indicate  $Z$  at half-filling obtained by IPT, IPT + FLEX, IPT + parquet, and CT-QMC, respectively. (b) The green, blue, and red lines indicate  $Z$  for  $U/t = 4, 8, 12$ , respectively. The open square corresponds to modified-IPT, solid square IPT + parquet, and the circle CT-QMC. The temperature is  $T/t = 0.04$  in both figures.

correlation effects. The quasiparticle weight is defined as

$$Z_\alpha = \left( 1 - \frac{\text{Im} \Sigma_{\alpha\alpha}(\omega_n)}{\omega_n} \Big|_{\omega_n \rightarrow 0} \right)^{-1}. \quad (39)$$

$Z_\alpha$  is roughly proportional to the inverse of the effective mass, and  $Z_\alpha = 0$  corresponds to the insulating state. In this study, however, we adopt the following definition instead of Eq. (39) for calculational simplicity:

$$Z_\alpha = \left( 1 - \frac{\text{Im} \Sigma_{\alpha\alpha}(\omega_n)}{\omega_n} \Big|_{n=0} \right)^{-1}. \quad (40)$$

Also, in this study, we adopt the definition of the band-filling  $n_\alpha [=T \sum_n G_{\alpha\alpha}(i\omega_n) e^{-i\omega_n 0}]$  as the number of electrons per site per spin.

### A. Single-orbital model

We study the square lattice model as a benchmark in the single-orbital systems. We set the temperature  $T/t = 0.04$  and we take  $64 \times 64$   $k$ -meshes and 4096 Matsubara frequencies, where  $t$  is the nearest-neighbor hopping. Figure 5 shows the quasiparticle weight calculated by several methods as a function of (a) the interaction  $U$  and (b) the band-filling  $n$ . IPT + FLEX is the method in which  $F_0$  in Sec. III A is obtained by the fluctuation exchange (FLEX) approximation [40]. In CT-QMC calculation, we use the CTHYB [4,6,42–45] code based on the TRIQS library [46]. We find that the result of IPT + parquet is the closest to that of the numerically exact CT-QMC. On the other hand,  $Z$  is overestimated in IPT and underestimated in IPT + FLEX since the two-particle fluctuations are underestimated in IPT and overestimated in IPT + FLEX. This quantitative improvement from (conventional) IPT is purely due to adding the diagonal terms estimated by parquet equations since the modified parameters are the same ( $A = 1, B = 0$ ) in both IPT and IPT + parquet. In Fig. 5(b),  $Z$ 's calculated by IPT, IPT + parquet, and CT-QMC are plotted as functions of the band filling  $n$  for  $U/t = 4, 8, 12$ . In the region away from half-filling, IPT + parquet tends to underestimate  $Z$  (overestimate the correlation effect) compared to IPT.

### B. Two-orbital model

Here, we study the two-orbital (single-site) model. The one body part of the Hamiltonian is expressed as

$$H_0 = \sum_{ij} \sum_{\alpha\beta} t_{ij,\alpha\beta} c_{i\alpha}^\dagger c_{j\beta} - \mu \sum_i \sum_\alpha n_{i\alpha}. \quad (41)$$

The interaction part of the Hamiltonian is expressed as

$$H_{\text{int}} = \sum_l U n_{l\uparrow} n_{l\downarrow} + \sum_{l_1 \neq l_2} \sum_{\sigma_1 \sigma_2} U' n_{l_1 \sigma_1} n_{l_2 \sigma_2} + \sum_{l_1 l_2} J \mathbf{S}_{l_1} \cdot \mathbf{S}_{l_2} + \sum_{l_1 l_2} J' c_{l_1 \uparrow}^\dagger c_{l_2 \downarrow}^\dagger c_{l_2 \downarrow} c_{l_1 \uparrow}, \quad (42)$$

where the degrees of freedom of orbital are expressed by  $l$  and spin by  $\sigma$ .  $U^{(l)}$  is the intraorbital (interorbital) interaction, and  $J$  and  $J'$  represent the Hund's coupling and pair hopping, respectively. Then the interaction matrices in the charge and spin channels are expressed as

$$(U_{l_1 l_2 l_3 l_4}^c, U_{l_1 l_2 l_3 l_4}^s) = \begin{cases} (U, U) & (l_1 = l_2 = l_3 = l_4), \\ (2U' - J, J) & (l_1 = l_2 \neq l_3 = l_4), \\ (2J - U', U') & (l_1 = l_3 \neq l_2 = l_4), \\ (J', J') & (l_1 = l_4 \neq l_2 = l_3). \end{cases} \quad (43)$$

Figure 6 shows the noninteracting density of states of the models which we study here.

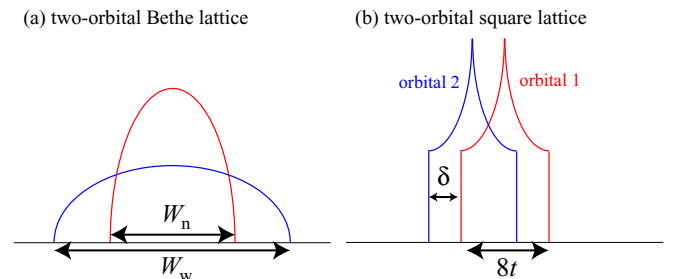


FIG. 6. The noninteracting density of states of the models. Left and right panels show the density of states of two-orbital Bethe lattice and two-orbital square lattice, respectively.

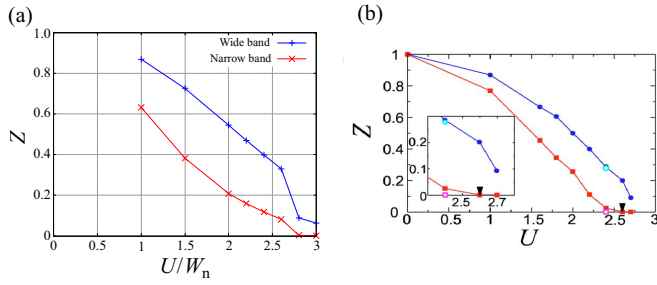


FIG. 7. Quasiparticle weight  $Z$  of the two-orbital Bethe lattice as a function of the interaction  $U$ . The temperature is  $T/W_n = 0.02$ . The result of IPT + parquet is shown in (a), and projective-QMC in (b). (This figure is taken from Ref. [47]). Red and blue lines indicate the narrow band and wide band, respectively.

### 1. Two-orbital Bethe lattice

We consider the two-orbital Bethe lattice model in which two bands with different bandwidth exist. We set  $W_w/W_n = 2$ , where  $W_n$  and  $W_w$  represent the half bandwidth of the narrow and wide bands, respectively. We also set  $U' = U - 2J$ ,  $J = U/4$ ,  $J' = 0$ , and the temperature  $T/W_n = 0.02$ . We take 2000 real-frequency meshes and 4096 Matsubara frequencies. The quasiparticle weight against the interaction  $U$  for each orbital is plotted in Fig. 7. Figure 7(a) is the result of IPT + parquet and Fig. 7(b) is that of the projective-QMC (PQMC) in Ref. [47]. We can see a good agreement between the two methods. The orbital selective Mott transition, in which the energy gap opens in the narrow band whereas the wide band is still metallic, occurs at  $U/W_n \sim 2.7$ .

### 2. Two-orbital square lattice

We study the two-orbital square lattice model which has only the intraorbital nearest-neighbor hopping. Here, we compare three impurity solvers: IPT + parquet, CT-QMC, and MO-IPT. In the CT-QMC calculation, we use the CTHYB package [4,6,42–45] based on the TRIQS library [46]. In the MO-IPT calculation, the spin-flip and the pair-hopping processes are ignored since MO-IPT supports only the density-density type interactions [27]. We set  $t_1 = t_2 = t$ , where  $t_\alpha = t_{i,i+1,\alpha}$  is the nearest-neighbor hopping of orbital  $\alpha$  and  $t$  is the unit of energy. The on-site energy difference  $\delta = t_{ii,11} - t_{ii,22}$ , and the interactions  $U' = U - 2J$ ,  $J = J' = U/4$ . We take  $32 \times 32$   $k$ -meshes and 4096 Matsubara frequencies and we fix the temperature  $T/t = 0.2$ . Here, we intentionally omitted the calculation result for half-filling, which turns out to require special care due to spontaneous symmetry breaking. This point will be studied in detail in a separate publication.

We start with the  $\delta = 0$  case (orbital degenerate case). Figure 8 shows the quasiparticle weight  $Z$  obtained by three methods MO-IPT, IPT + parquet, and CT-QMC as a function of the filling  $n$  for several interaction strength  $U$  at  $\delta = 0$ . Since the two orbitals are equivalent at  $\delta = 0$ , we show only the  $Z$  of orbital 1 and omit the orbital index. The MO-IPT results significantly deviate from those of CT-QMC, which is qualitatively consistent with the situation for the two-orbital Bethe lattice model in Ref. [27]. By contrast, the  $Z$  of IPT + parquet agrees well with that of CT-QMC.

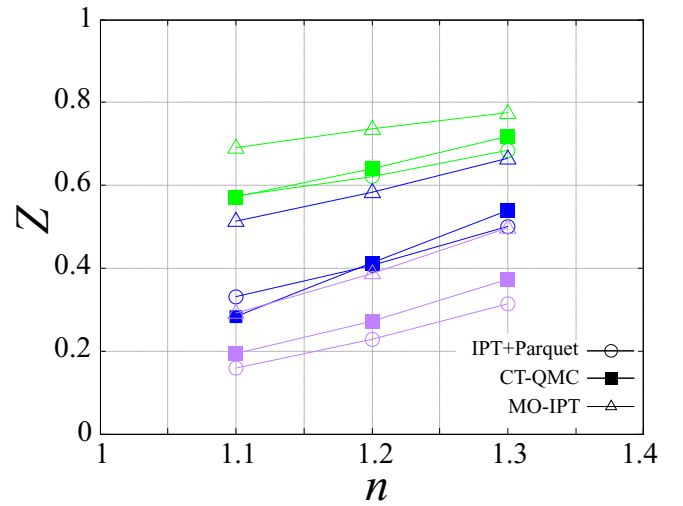


FIG. 8. Quasiparticle weight  $Z$  of the two-orbital square lattice as a function of the band filling  $n$ . The temperature is  $T/t = 0.2$  and the on-site energy difference is  $\delta/t = 0$ . Green, blue, and purple lines indicate the results at  $U/t = 4, 6$ , and  $10$ , respectively. Circle, square, and triangle represent IPT + parquet, CT-QMC, and MO-IPT, respectively.

We move on to the  $\delta/t = 1.6$  case (orbital nondegenerate case). Figure 9 shows the quasiparticle weight  $Z$  at  $\delta/t = 1.6$ . The deviations of  $Z$ 's of MO-IPT from that of CT-QMC are largely different between the two orbitals [48]. IPT + parquet is found to improve the situation. This improvement comes from adding the degree-of-freedom to the pseudochemical potential  $\mu_0$ , which enables the IPT + parquet method to capture the strong correlation effects more appropriately in both orbitals as explained in Sec. III A. Figure 10(a) shows the correlation part of the self-energy  $\Sigma^{\text{CR}}(i\omega_n)$  obtained by these three methods. We can see that  $\Sigma^{\text{CR}}(i\omega_n)$  of IPT + parquet shows better agreement with CT-QMC than MO-IPT, not only in orbital 2 but also in orbital 1, and not only in the imaginary part which contributes the quasiparticle weight  $Z$  but also in the real part. Figures 10(b) and 10(c) show the spectral function  $A(\omega)$  obtained by performing the analytic continuation with a Padé approximation in IPT + parquet and MO-IPT, and with Maximum entropy method using the  $\Omega$  MAXENT code [49] in CT-QMC. Similarly to  $\Sigma^{\text{CR}}(i\omega_n)$ ,  $A(\omega)$  of IPT + parquet shows better agreement with that of CT-QMC. Especially at  $n = 1.1$ , IPT + parquet shows an improvement from MO-IPT.

### C. Bilayer model

Here, we study the bilayer model on the square lattice as a benchmark of systems with multiple sites (with one orbital per site) in a unit cell. The Hamiltonian of this model is expressed as

$$H = \sum_{(ij)} \sum_{\alpha} t c_{i\alpha}^{\dagger} c_{j\alpha} + \sum_i \sum_{\alpha \neq \beta} t_{\perp} c_{i\alpha}^{\dagger} c_{i\beta} + \sum_i \sum_{\alpha} U n_{i\alpha} n_{i\alpha}, \quad (44)$$

where  $t$  ( $t_{\perp}$ ) represents the intralayer (interlayer) hopping and  $U$  the on-site interaction. The temperature is fixed as  $T/t = 0.2$ , and the hopping ratio  $t_{\perp}/t = 1.0$ . We take  $32 \times 32$

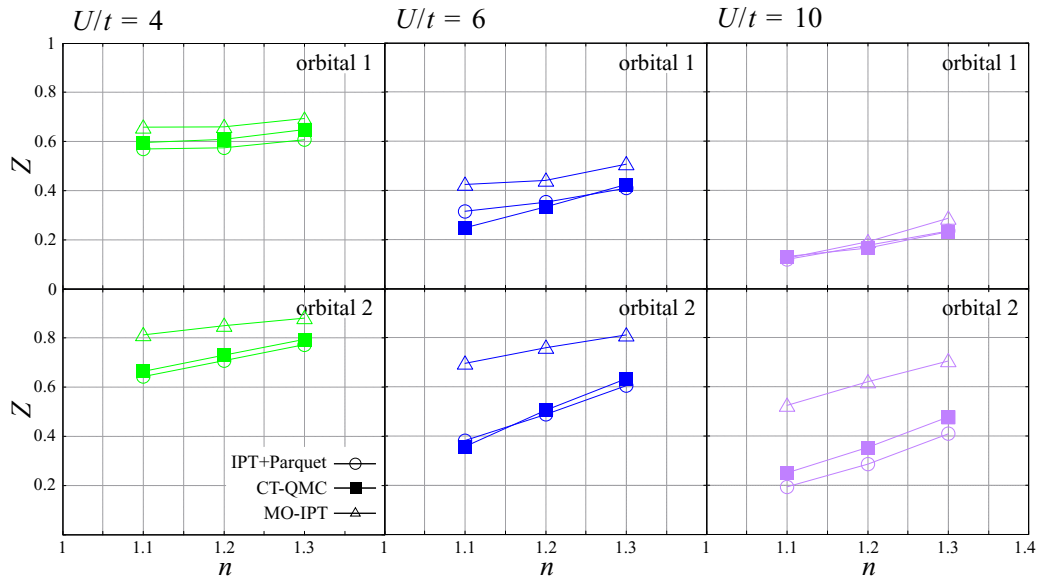


FIG. 9. Quasiparticle weight  $Z$  of the two-orbital square lattice as a function of the band filling  $n$ . The temperature is  $T/t = 0.2$  and the on-site energy difference is  $\delta/t = 1.6$ . Green, blue, and purple lines indicate the results at  $U/t = 4, 6,$  and  $10$ , respectively. Circle, square, and triangle represent IPT + parquet, CT-QMC, and MO-IPT, respectively.

$k$ -meshes and 4096 Matsubara frequencies. Since the two sites are equivalent in this model, we show only the quantities of site 1 and omit the site index. The quasiparticle weight  $Z$  is plotted in Fig. 11. When  $U/t = 4$ , MO-IPT shows better agreement with CT-QMC than IPT + parquet. When  $U$  is increased, we can see the tendency that CT-QMC agrees with IPT + parquet (MO-IPT) near (away from) half-filling, similarly to the single-orbital case in Sec. IV A. Figure 12(a) shows the correlation part of the self-energy  $\Sigma^{\text{CR}}(i\omega_n)$  with  $U/t = 8$ . As we can also see from  $Z$ , IPT + parquet shows better agreement with CT-QMC at  $n = 1.0$ . At  $n = 1.2$ , the agreement between MO-IPT and CT-QMC is better in the imaginary part whereas the agreement between IPT + parquet and CT-QMC is better in the real part. In this model, the modified parameters  $\mu_0, A, B$  are the same between IPT + parquet and MO-IPT since the two sites are equivalent and only the on-site interaction is considered (the interaction matrix has no off-diagonal part in terms of degree-of-freedom). So the differences come from the two-particle fluctuation and the off-diagonal part of self-energy, which are not considered in MO-IPT. Figures 12(b) and 12(c) show the spectral function  $A(\omega)$  with  $U/t = 8$ . IPT + parquet shows better agreement with CT-QMC at  $n = 1.0$ . At  $n = 1.2$ , CT-QMC and MO-IPT show better agreement in terms of the width of the central peak whereas CT-QMC and IPT + parquet show better agreement in terms of the shape of  $A(\omega)$ . This reflects the fact that the imaginary part of the Matsubara self-energy is mainly related to the strength of renormalization [width of the central peak of  $A(\omega)$ ] and the real part is related to the electron-hole asymmetry.

## V. DISCUSSION

### A. Validity and advantage

Here, we discuss the validity and the advantage of the IPT + parquet method. The full vertex in the IPT + parquet

method is represented by a simple product of functions as in Eqs. (28) and (35). This simple product form of the full vertex can be justified to some extent by considering the nature of the two-particle functions, which are ingredients of the diagrams that give contributions of the cross and central structures. We can also find that the validity of this simple product form of the full vertex becomes higher when the contributions of diagrams which give the cross and central structures become larger (see Appendix B for details). In the single-orbital case, indeed, we can see this simple product form of the full vertex in the atomic limit (see Appendix C).

Comparing with the existing IPT formalisms, the IPT + parquet method has the following advantages. (i) In the IPT + parquet method, the dynamical effects of the two-particle bosonic fluctuation in the full vertex, which give the diagonal structure and are more important in the multiband systems, are taken into account, whereas these are not treated in the IPT. (ii) It is easy to apply diagrammatic extensions of DMFT for the nonlocal correlation. In the IPT + parquet method, since the two-particle fluctuations in each channel (ph, ph,pp) in the full vertex are estimated with a physically reasonable method (the parquet formalism), we can calculate the two-particle quantities necessary for diagrammatic extensions from this full vertex (we show this point in a separate publication. Ref. [41]). On the contrary, in IPT, since there is no perspective on the two-particle fluctuations in the full vertex, it is difficult to estimate the two-particle quantities. Although a method to reconstruct the full vertex in IPT has been suggested in single-band systems [50], it cannot be used in multiband systems.

IPT + parquet has a great advantage over CT-QMC in terms of the computational efficiency. We compare the cost of IPT + parquet with that of CT-QMC, employing the “core hours” [51] as an indicator of numerical costs. The order of core hours of IPT + parquet is  $O(1)$  and CT-QMC  $O(10^2)$  in two-band cases. The difference between the costs of the two



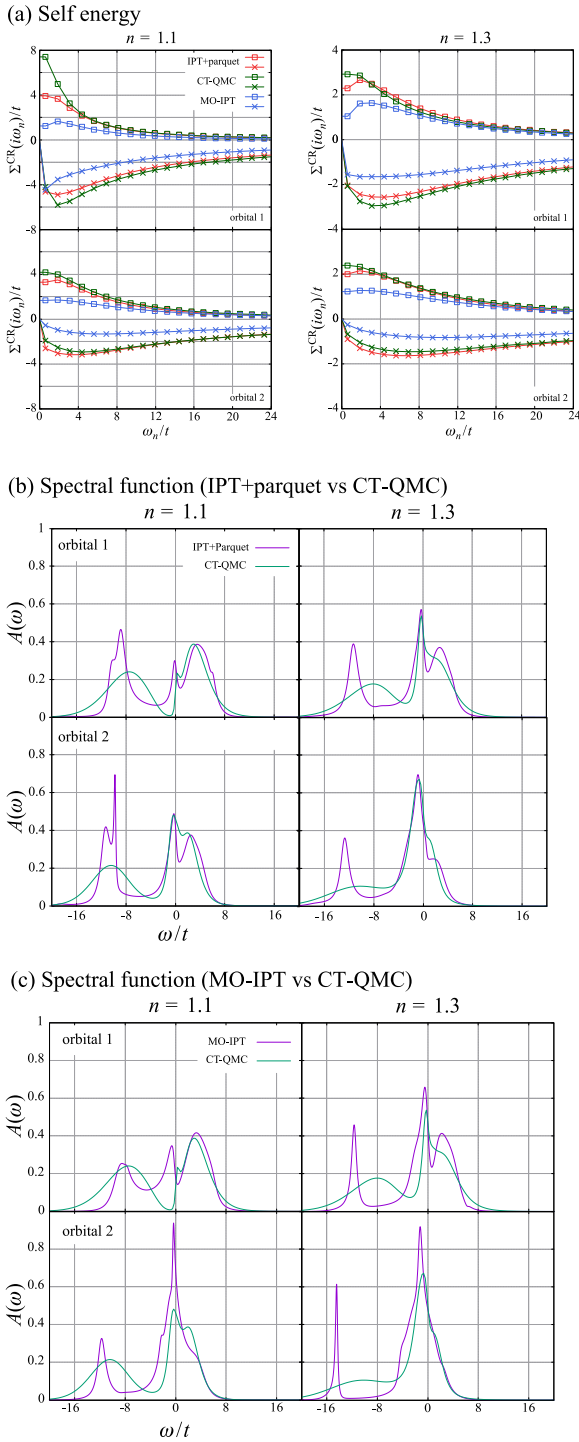


FIG. 10. (a) The correlation part of the self-energy  $\Sigma^{\text{CR}}(\omega)$  of the two-orbital square lattice.  $\Sigma^{\text{CR}}(i\omega_n)$  of orbital 1 is shown in upper panel and orbital 2 in lower panel. Square and cross symbols indicate the real and imaginary parts, respectively. Red, green, and blue lines indicate  $\Sigma^{\text{CR}}(i\omega_n)$  obtained by IPT + parquet, CT-QMC, and MO-IPT, respectively. (b,c) Spectral function  $A(\omega)$  of the two-orbital square lattice for several fillings. Interaction strength is  $U/t = 10$ . The spectral function  $A(\omega)$  of orbital 1 is shown in upper panel and orbital 2 in lower panel. Purple lines indicate  $A(\omega)$  obtained by (b) IPT + parquet and (c) MO-IPT. Green lines indicate  $A(\omega)$  obtained by CT-QMC. The temperature is  $T/t = 0.2$ , and the on-site energy difference is  $\delta/t = 1.6$ .

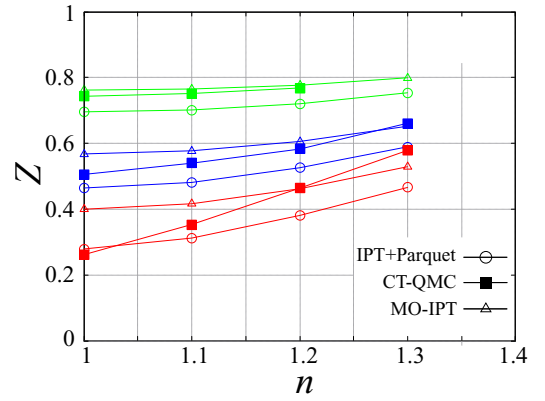


FIG. 11. Quasiparticle weight  $Z$  of the bilayer model as a function of the interaction  $n$ . Green, blue, and red lines indicate the results at  $U/t = 4, 6, 8$ , respectively. Circle, square, and triangle represent IPT + parquet, CT-QMC, and MO-IPT, respectively.

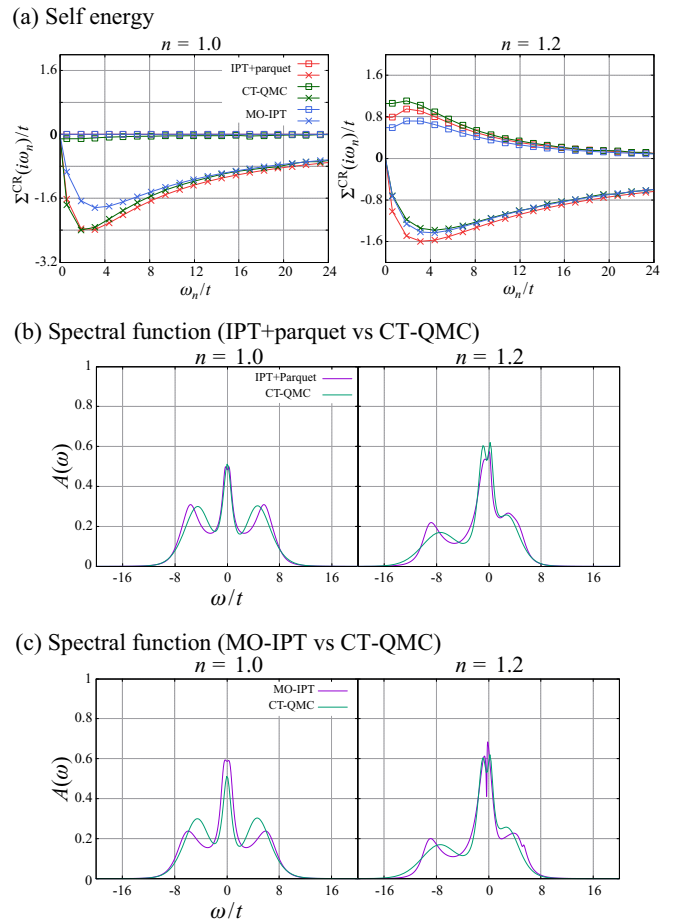


FIG. 12. (a) The correlation part of the self-energy  $\Sigma^{\text{CR}}(\omega)$  of the bilayer model. Square and cross symbols indicate the real and imaginary parts, respectively. Red, green, and blue lines indicate  $\Sigma^{\text{CR}}(i\omega_n)$  obtained by IPT + parquet, CT-QMC, and MO-IPT, respectively. (b,c) Spectral function  $A(\omega)$  of the bilayer model for several fillings. Purple lines indicate  $A(\omega)$  obtained by (b) IPT + parquet and (c) MO-IPT. Green lines indicate  $A(\omega)$  obtained by CT-QMC. Interaction strength is  $U/t = 8$ , the temperature  $T/t = 0.2$ , and the ratio of hoppings  $t_{\perp}/t = 1.0$ .

methods may increase when we apply these to a system which has the larger degrees of freedom or is more realistic. The CT-QMC simulations can suffer from the sign problem in these systems and need more and more samplings to obtain reliable results while IPT + parquet does not have these difficulties.

### B. Scopes of applications of MO-IPT and IPT + parquet

Here, we discuss the scopes of application of MO-IPT and IPT + parquet from the results of this study and the previous MO-IPT benchmark [27].

First, we discuss the orbital degenerate systems with the interaction having only the intraorbital elements. The covalent insulator model in Sec. 3.3 in Ref. [27] and the bilayer model in Sec. IV C in this study correspond to these systems. In these systems, both MO-IPT and IPT + parquet show good agreements with the numerically exact CT-QMC. As shown in Sec. IV C, IPT + parquet (MO-IPT) is better near (away from) half-filling.

Next, we discuss the orbital degenerate systems with both intra and interorbital interactions. The two-orbital Bethe lattice model in Secs. 3.4.1 and 3.4.2 of Ref. [27] and the two-orbital square lattice model in Sec. IV B 2 of our study correspond to these systems. As shown in Ref. [27] and also in Sec. IV B 2 of our study, the MO-IPT results significantly deviate from that of the CT-QMC results at or near half filling. This may be due to the drawback of the approximation in the modified parameter  $B_\alpha$  in Eq. (A13). The calculation results lose electron-hole symmetry even in situations where the symmetry should be present since  $B = 0$ , which is the condition required in electron-hole symmetric systems (see Appendix E for details), is not satisfied. Another version of MO-IPT [26], which was developed by Laad *et al.* and has been applied to realistic systems [52–57], does not have this drawback. Hence, systematic benchmarks of this version of MO-IPT for simple models, which have not been performed to our knowledge, are desired. If this version of MO-IPT turns out to also give results that deviate from CT-QMC at or near half-filling, it may imply the limitations of the correction to modified parameters  $A, B$  by the static many-particle correlation functions. On the other hand, the IPT + parquet, in which the many-particle correlation effects are considered as dynamical functions obtained by the parquet equations, agrees well with CT-QMC at or near half-filling, as shown for the orbital-degenerate cases of the two-orbital square lattice and two-orbital Bethe lattice models in Secs. IV B 2 and IV B 1, respectively.

Finally, we discuss the orbital nondegenerate systems which correspond to the two-orbital square lattice model in Sec. IV B 2 [58]. As mentioned in Sec. IV B 2, a remarkable feature in this situation is that the deviations of MO-IPT from CT-QMC are largely different between the two orbitals. Namely, MO-IPT fails to appropriately describe the correlation effects near half-filling that can depend on the orbitals when the orbitals are nonequivalent. This can be understood from the new interpretation introduced in Sec. III. As explained in Sec. III C,  $n_{0\alpha} = n_\alpha$  needs to be satisfied to estimate the correlation effects appropriately in each orbital. However, in MO-IPT,  $n_{0\alpha}$  and  $n_\alpha$  do not satisfy this condition. We overcome this difficulty by adding a degree of freedom to the

pseudochemical potential  $\mu_0$  in IPT + parquet. As a result, the IPT + parquet agrees well with CT-QMC also in nondegenerate systems.

## VI. CONCLUSION

We have reinterpreted IPT as an approximation which captures the strong correlation effects by the mimicking the cross and central structures of the exact full vertex and extended it such that it can be applied to the multiband systems. We have validated this method (IPT + parquet) by comparing it with the numerically exact CT-QMC method. As a result, we have confirmed that the results of IPT + parquet show good agreement with that of CT-QMC not only in the single-band systems but also in the multiband systems. In addition, numerical costs are largely reduced: core hours of IPT + parquet are at least 100 times smaller than that of CT-QMC. We expect that IPT + parquet can be useful for analyzing various multiband and strongly correlated systems.

## ACKNOWLEDGMENTS

Part of the numerical calculations was performed using the large-scale computer systems provided by the following institutions: The supercomputer center of the Institute for Solid State Physics, the University of Tokyo, and the Information Technology Center, the University of Tokyo. This study has been supported by JSPS KAKENHI Grant No. JP18H01860.

## APPENDIX A: OUTLINE OF DMFT AND IPT SOLVER

### 1. DMFT

DMFT is based on the equivalency between two models which is exact in the limit of the infinite spatial dimension  $d \rightarrow \infty$ . In the finite spatial dimension case, DMFT can be considered as the approximation in which the temporal fluctuation is treated correctly while ignoring the spatial fluctuation.

In DMFT, the lattice problem is solved by mapping it onto an impurity problem. The lattice model (Hubbard model) is given in Eq. (1). The Anderson impurity model for multiband systems is described as

$$H = \sum_{\mathbf{k}} \sum_{\alpha\beta} \epsilon_{\mathbf{k}\alpha\beta} b_{\mathbf{k}\alpha}^\dagger b_{\mathbf{k}\beta} + \sum_{\mathbf{k}} \sum_{\alpha\beta} (V_{\mathbf{k}\alpha\beta} b_{\mathbf{k}\alpha}^\dagger f_\beta + \text{H.c.}) + \sum_{\alpha\beta} \epsilon_{f\alpha\beta} f_\alpha^\dagger f_\beta + \frac{1}{4} \sum_{\alpha\beta\gamma\lambda} U_{\alpha\beta\gamma\lambda} f_\alpha^\dagger f_\lambda^\dagger f_\gamma f_\beta, \quad (\text{A1})$$

where  $b_{\mathbf{k}\alpha}^{(\dagger)}$  is the annihilation (creation) operator for bath electrons and  $f_\alpha^{(\dagger)}$  for impurity electrons.  $\epsilon_{\mathbf{k}\alpha\beta}$  and  $\epsilon_{f\alpha\beta}$  are the energy of bath and impurity electrons, respectively.  $V_{\mathbf{k}\alpha\beta}$  is the hybridization strength of the bath and impurity electrons and  $U_{\alpha\beta\gamma\lambda}$  is the interaction in the impurity site. The Green's function in the Hubbard model can be written as

$$\hat{G}_{\text{lat}}(\mathbf{k}) = [(i\omega_n + \mu)\hat{I} - \hat{\epsilon}_{\mathbf{k}} - \hat{\Sigma}(i\omega_n)]^{-1}, \quad (\text{A2})$$

where the spatial fluctuation ( $\mathbf{k}$  dependence of the self-energy) is ignored. Also, the Green's function in the impurity model

can be written as

$$\hat{G}_{\text{imp}}(i\omega_n) = [(i\omega_n + \mu)\hat{I} - \hat{\epsilon}_f - \hat{\Delta}(i\omega_n) - \hat{\Sigma}(i\omega_n)]^{-1}, \quad (\text{A3})$$

where  $\Delta(i\omega_n) = N_k^{-1} \sum_k V_k(i\omega_n - \epsilon_k)^{-1} V_k$  is the hybridization function. The self-consistent condition in DMFT is given by

$$\hat{\Delta}(i\omega_n) = (i\omega_n + \mu)\hat{I} - \hat{\Sigma}(i\omega_n) - \left( \sum_k \hat{G}_{\text{lat}}(k) \right)^{-1}. \quad (\text{A4})$$

Although there are small differences depending on the impurity solvers, the actual calculation procedure in DMFT is roughly as follows.

- (1) Start from an initial guess for the self-energy  $\Sigma(i\omega_n)$ .
- (2) Calculate the lattice Green's function  $G_{\text{lat}}(k)$  by Eq. (A3).
- (3) Calculate the hybridization function  $\Delta(i\omega_n)$  by Eq. (A4).
- (4) Solve the impurity problem using  $\Delta(i\omega_n)$  and obtain the new self-energy.
- (5) Go back to step 2 (iterate until convergence).

Various methods to solve the impurity problem (step 4) have been proposed [4–6,8,9,11,12,16–27,59,60], and they are called impurity solvers. We introduce two impurity solvers we use in this study in the following section.

## 2. Iterative perturbation theory

In the iterative perturbation theory (IPT) [16–20], the correlation part of the self-energy is approximated by the second-order perturbation, i.e.,

$$\Sigma(i\omega_n) = \Sigma^{\text{HF}} + \Sigma^{\text{CR}}(i\omega_n), \quad (\text{A5})$$

$$\Sigma^{\text{CR}}(i\omega_n) \approx \Sigma^{\text{2nd}}(i\omega_n) = T \sum_{\nu_m} U \chi_0(i\nu_m) U G_0(i\omega_n + i\nu_m), \quad (\text{A6})$$

$$\chi_0(i\nu_m) = -T \sum_n G_0(i\omega_n) G_0(i\omega_n + i\nu_m), \quad (\text{A7})$$

$$G_0(i\omega_n) = [i\omega_n + \mu_0 - \Delta(i\omega_n) - \Sigma^{\text{HF}}]^{-1}, \quad (\text{A8})$$

where  $\Sigma^{\text{HF}}$  is the Hartree-Fock term (mean-field term) and  $\Sigma^{\text{CR}}(i\omega_n)$  the correlation term of the self-energy,  $\Delta(i\omega)$  the hybridization function,  $\mu_0$  the pseudochemical potential. In the electron-hole symmetric case, IPT provides a good result in both weak and strong correlation regimes. Especially in the strong correlation limit, the IPT self-energy reproduces the exact solution even though it is a perturbation solution from the weak coupling limit. In other cases, however, the results are not so good. To overcome this weakness, modified-IPT [21–23] was proposed as an extended version of IPT for arbitrary filling. In the modified-IPT, the correlation part of the self-energy is parametrized by

$$\Sigma^{\text{CR}}(i\omega_n) = \frac{A \Sigma^{\text{2nd}}(i\omega_n)}{1 - B \Sigma^{\text{2nd}}(i\omega_n)}. \quad (\text{A9})$$

The constants  $A$  and  $B$  are determined such that one reproduces the exact solutions in the high frequency and atomic

limits:

$$A = \frac{n(1-n)}{n_0(1-n_0)}, \quad B = \frac{(1-2n)U + \mu_0 - \mu}{n_0(1-n_0)U^2}, \quad (\text{A10})$$

where  $n_0$  and  $n$  are the electron numbers evaluated from  $G_0(i\omega_n)$  and  $G(i\omega_n)$ , respectively. The chemical potential  $\mu$  is determined by fixing  $n$  at the input value, while the pseudochemical potential  $\mu_0$  is a free parameter. Various conditions for determining  $\mu_0$  have been suggested: Luttinger sum rule,  $n = n_0$ , and so on [21–23]. Hereafter, if we write IPT, it refers to modified-IPT.

Furthermore, some extended versions of the modified-IPT for multiorbital systems have been proposed [24–27]. Here, we summarize the outline of the MO-IPT developed in Ref. [27], which is the latest version of these methods, with a slight modification. In the MO-IPT, the orbital-diagonal parts of the self-energy are parametrized as

$$\Sigma_{\alpha\alpha}^{\text{CR}}(i\omega_n) = \frac{A_{\alpha} \Sigma_{\alpha\alpha}^{\text{2nd}}(i\omega_n)}{1 - B_{\alpha} \Sigma_{\alpha\alpha}^{\text{2nd}}(i\omega_n)}, \quad (\text{A11})$$

where  $\alpha$  indicates the degrees of freedom of spin and orbital. Here, off-diagonal parts are ignored. Similarly to the single-orbital case,  $A_{\alpha}$  is determined such that one reproduces the exact solution in the high-frequency limit. On the other hand,  $B_{\alpha}$  is determined such that one reproduces the approximate solution in the atomic limit since the exact solution can not be written in a simple form in multiorbital systems. Namely,

$$A_{\alpha} = \frac{1}{\tau_{\alpha}} \sum_{\beta \neq \alpha} U_{\alpha\beta} \langle n_{\beta} \rangle (1 - \langle n_{\beta} \rangle) U_{\beta\alpha} + \frac{1}{\tau_{\alpha}} \sum_{\beta \neq \alpha} \sum_{\gamma \neq \beta \neq \alpha} U_{\alpha\beta} \langle n_{\beta} n_{\gamma} \rangle - \langle n_{\beta} \rangle \langle n_{\gamma} \rangle U_{\gamma\alpha}, \quad (\text{A12})$$

$$B_{\alpha} = \frac{1}{\tau_{\alpha}} \left( \mu_0 - \mu - 2 \sum_{\beta (\neq \alpha)} U_{\alpha\beta} \langle n_{\beta} \rangle \right) + \frac{1}{\tau_{\alpha}^2 A_{\alpha}} \sum_{\beta \gamma \eta (\neq \alpha)} U_{\alpha\beta} U_{\alpha\gamma} U_{\alpha\eta} (\langle n_{\beta} n_{\gamma} n_{\eta} \rangle - \langle n_{\beta} \rangle \langle n_{\gamma} n_{\eta} \rangle), \quad (\text{A13})$$

$$\tau_{\alpha} = \sum_{\beta} U_{\alpha\beta} \langle n_{0\beta} \rangle (1 - \langle n_{0\beta} \rangle) U_{\beta\alpha}, \quad (\text{A14})$$

where  $U_{\alpha\beta} = U_{\alpha\alpha\beta\beta}$ . The difference between Eq. (A13) and Eq. (A.22) in Ref. [27] is due to the difference between the notations of the zeroth-order Green's function. Adopting the Matsubara frequency formalism, we impose the condition  $n_{0\text{total}} = n_{\text{total}}$  to fix  $\mu_0$ , where  $n_{0\text{total}}$  and  $n_{\text{total}}$  are the total electron density obtained from  $G_0$  and  $G$ , while the real frequency is used in Ref. [27] and  $\mu_0$  is determined such that the Luttinger theorem is satisfied. We confirmed that the results are nearly independent of the adopted frequency types or conditions for  $\mu_0$ , by performing calculations for several models studied in Ref. [27].

## APPENDIX B: DIAGRAMMATIC ORIGINS OF CROSS AND CENTRAL STRUCTURES

Here, we show the diagrammatic origins of the cross and central structures. First, we explain the cross structure. The

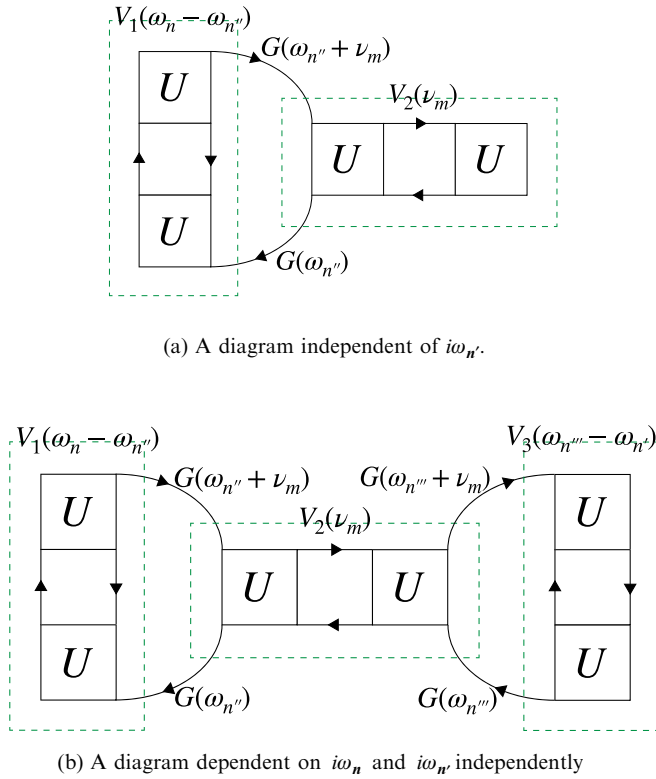


FIG. 13. Examples of diagrams for each frequency structure. The diagrams depicted in (a) and (b) give the cross and central structures, respectively.

combination of some channels depicted in Fig. 13(a), which extinguishes the  $\omega_n$  or  $\omega_{n'}$  dependence of  $F^c(i\omega_n, i\omega_{n'}, i\nu_m)$  as follows:

$$T \sum_{n''} V_1(\omega_n - \omega_{n''}) G(\omega_{n''} + \nu_m) G(\omega_{n''}) V_2(\nu_m). \quad (\text{B1})$$

This contribution make  $F^c(i\omega_n, i\omega_{n'}, i\nu_m)$  take large values in the vicinity of  $\omega_n = 0$  and  $\omega_{n'} = 0$  lines. Next, we explain the central structure. The multiple combinations of some channels depicted in Fig. 13(b) yields the contribution which depends on  $\omega_n$  and  $\omega_{n'}$  independently as

$$T^2 \sum_{n'', n'''} V_1(\omega_n - \omega_{n''}) G(\omega_{n''} + \nu_m) G(\omega_{n''}) \times V_2(\nu_m) G(\omega_{n'''} + \nu_m) G(\omega_{n'''}) V_3(\omega_{n'''} - \omega_{n'}). \quad (\text{B2})$$

This makes  $F^c(i\omega_n, i\omega_{n'}, i\nu_m)$  take large values in the center of  $n$ - $n'$  plane.

As we can see from its origin, the cross or central structures come from the higher-order diagrams than that of the diagonal structure. Therefore these contributions are important in the strongly correlated regime.

Also, we can show that the simple product form of the full vertex in Eqs. (28) and (35) is reasonable to some extent by considering the nature of the two-particle functions which transfer the bosonic frequencies  $\nu_m$ . For example,  $V_i(\nu_m)$  in Eq. (B1) or Eq. (B2) has a large value in the vicinity of  $\nu_m = 0$  and becomes similar to the  $\delta$  function when the two-particle fluctuation becomes large. As an extreme case, if we approx-

imate  $V_1$  and  $V_3$  by the  $\delta$  function in Eq. (B1) or Eq. (B2), we obtain the frequency dependence of ph part in Eqs. (28) and (35).

### APPENDIX C: FULL VERTEX IN THE ATOMIC LIMIT

In the case of single-band systems, we can write down the full vertex in the atomic limit as follows [29]:

$$F_{\text{atom}}^{c,s} = F_{\text{atom}}^{\uparrow\uparrow} \pm F_{\text{atom}}^{\uparrow\downarrow}, \quad (\text{C1})$$

$$F_{\text{atom}}^{\uparrow\uparrow} = -\beta \frac{U^2}{4} (\delta_{\omega_n \omega_{n'}} - \delta_{\nu_m 0}) - \beta \frac{U^4}{16} (\delta_{\omega_n \omega_{n'}} - \delta_{\nu_m 0}) \left( \frac{1}{\omega_n^2} + \frac{1}{(\omega_{n'} + \nu_m)^2} \right) - \beta \frac{U^6}{64} \frac{\delta_{\omega_n \omega_{n'}} - \delta_{\nu_m 0}}{\omega_n^2 (\omega_{n'} + \nu_m)^2}, \quad (\text{C2})$$

$$F_{\text{atom}}^{\uparrow\downarrow} = U + \beta \frac{U^2}{4} \left[ \frac{2\delta_{\omega_n(-\omega_{n'} - \nu_m)} + \delta_{\nu_m 0}}{1 + e^{\beta U/2}} - \frac{2\delta_{\omega_n \omega_{n'}} + \delta_{\nu_m 0}}{1 + e^{-\beta U/2}} \right] + \frac{U^3}{8} \frac{\omega_n^2 + (\omega_n + \nu_m)^2 + (\omega_{n'} + \nu_m)^2 + \omega_{n'}^2}{\omega_n (\omega_n + \nu_m) (\omega_{n'} + \nu_m) \omega_{n'}} + \beta \frac{U^4}{16} \left[ \frac{2\delta_{\omega_n(-\omega_{n'} - \nu_m)} + \delta_{\nu_m 0}}{1 + e^{\beta U/2}} \times \left( \frac{1}{(\omega_n + \nu_m)^2} + \frac{1}{(\omega_{n'} + \nu_m)^2} \right) - \frac{2\delta_{\omega_n \omega_{n'}} + \delta_{\nu_m 0}}{1 + e^{-\beta U/2}} \left( \frac{1}{\omega_n^2} + \frac{1}{(\omega_{n'} + \nu_m)^2} \right) \right] + \frac{3U^5}{16} \frac{1}{\omega_n (\omega_n + \nu_m) (\omega_{n'} + \nu_m) \omega_{n'}} + \beta \frac{U^6}{64} \left[ \frac{2\delta_{\omega_n(-\omega_{n'} - \nu_m)} + \delta_{\nu_m 0}}{1 + e^{\beta U/2}} \frac{1}{(\omega_n + \nu_m)^2 (\omega_{n'} + \nu_m)^2} - \frac{2\delta_{\omega_n \omega_{n'}} + \delta_{\nu_m 0}}{1 + e^{-\beta U/2}} \frac{1}{\omega_n^2 (\omega_{n'} + \nu_m)^2} \right]. \quad (\text{C3})$$

The structure of each order is as follows.

- (1)  $U^1 \rightarrow$  constant.
- (2)  $U^2 \rightarrow$  diagonal structure.
- (3)  $U^3 \rightarrow$  cross structure.
- (4)  $U^4 \rightarrow$  diagonal  $\times$  cross structure.
- (5)  $U^5, U^6 \rightarrow$  diagonal  $\times$  central structure.

We can indeed see that the diagonal structure is dominant in the small  $U$  regime and the cross and central structures develop as  $U$  increases.

### APPENDIX D: SIMPLIFIED PARQUET METHOD

In this section, we introduce the simplified parquet method developed in Ref. [32], in which the numerical cost is much lower than that of the nonsimplified parquet method since we should practically consider just one of the three variables ( $k, k', q$ ). Since the simplified parquet method in Ref. [32] has not been extended for multiband systems, we extend it for our purpose. We show here this multiband version of the simplified parquet method. There are differences between coefficients in Ref. [32] and in our notation. These come from



the difference in treatments of 1/2 factor which is needed to avoid the double counting of diagrams in the pp channel. This factor emerges in the definitions of the vertices in our notation while it emerges in the Bethe-Salpeter equation in Ref. [32]. Before we start introducing the simplified parquet method, we define the following notation which indicates the set of the degrees of freedom, the frequencies, and wave vectors:

$$D = (\alpha, \beta, \gamma, \lambda), (k, k', q), \quad (\text{D1})$$

$$C = (\alpha, \gamma, \beta, \lambda), (k, k + q, k' - k), \quad (\text{D2})$$

$$P = (\alpha, \lambda, \gamma, \beta), (k, k', -q - k - k'), \quad (\text{D3})$$

$$X = (\alpha, \gamma, \lambda, \beta), (k, -k - q, k' - k). \quad (\text{D4})$$

In the presence of SU(2) symmetry in spin space, the full vertex can be divided into four channels  $c$  (charge),  $s$  (spin),  $e$  (even), and  $o$  (odd) in terms of the parity of spin

$$F_r(D) = \Lambda_r(D) + \Phi_{\text{ph},r}(D) + \Phi_{\overline{\text{ph}},r}(D) + \Phi_{\text{pp},r}(D) \quad (r = c, s, e, o). \quad (\text{D5})$$

We can rewrite Eq. (D5) as follows by replacements of variables and indices:

$$F_c(D) = \Lambda_c(D) + \Phi_{\text{ph},c}(D) - \frac{1}{2}[\Phi_{\text{ph},c} + 3\Phi_{\text{ph},s}](C) + [\Phi_{\text{pp},e} - 3\Phi_{\text{pp},o}](P), \quad (\text{D6})$$

$$F_s(D) = \Lambda_s(D) + \Phi_{\text{ph},s}(D) - \frac{1}{2}[\Phi_{\text{ph},c} - \Phi_{\text{ph},s}](C) - [\Phi_{\text{pp},e} - \Phi_{\text{pp},o}](P), \quad (\text{D7})$$

$$F_e(D) = \Lambda_e(D) + \Phi_{\text{pp},e}(D) + \frac{1}{4}[\Phi_{\text{ph},c} - 3\Phi_{\text{ph},s}](X) + \frac{1}{4}[\Phi_{\text{ph},c} - 3\Phi_{\text{ph},s}](P), \quad (\text{D8})$$

$$F_o(D) = \Lambda_o(D) + \Phi_{\text{pp},o}(D) + \frac{1}{4}[\Phi_{\text{ph},c} + \Phi_{\text{ph},s}](X) - \frac{1}{4}[\Phi_{\text{ph},c} + \Phi_{\text{ph},s}](P). \quad (\text{D9})$$

As we can see from Eqs. (D6) to (D9), since  $c, s$  is always together with ph,  $e, o$  with pp, we omit the subscripts ph or pp hereafter. And we write the third and fourth term as  $\gamma_r^{(1)}$  and  $\gamma_r^{(2)}$ , respectively. To say,

$$\gamma_c^{(1)}(D) = -\frac{1}{2}[\Phi_c + 3\Phi_s](D), \quad (\text{D10})$$

$$\gamma_s^{(1)}(D) = -\frac{1}{2}[\Phi_c - \Phi_s](D), \quad (\text{D11})$$

$$\gamma_e^{(1)}(D) = \frac{1}{4}[\Phi_c - 3\Phi_s](D), \quad (\text{D12})$$

$$\gamma_o^{(1)}(D) = \frac{1}{4}[\Phi_c + \Phi_s](D), \quad (\text{D13})$$

$$\gamma_c^{(2)}(D) = [\Phi_e - 3\Phi_o](D), \quad (\text{D14})$$

$$\gamma_s^{(2)}(D) = -[\Phi_e - \Phi_o](D), \quad (\text{D15})$$

$$\gamma_e^{(2)}(D) = \frac{1}{4}[\Phi_c - 3\Phi_s](D), \quad (\text{D16})$$

$$\gamma_o^{(2)}(D) = -\frac{1}{4}[\Phi_c + \Phi_s](D). \quad (\text{D17})$$

We can also write the Bethe-Salpeter equation by using the four channels

$$\hat{F}_r = \hat{\Gamma}_r + \hat{\Phi}_r \quad (r = c, s, e, o), \quad (\text{D18})$$

$$\hat{\Phi}_r = -\hat{\Gamma}_r \hat{\chi}_0 \hat{F}_r = -\hat{\Gamma}_r \hat{\chi}_r \hat{\Gamma}_r, \quad (\text{D19})$$

and the susceptibilities

$$\hat{\chi}_r = \hat{\chi}_0 - \hat{\chi}_0 \hat{\Gamma}_r \hat{\chi}_r = \hat{\chi}_0 - \hat{\chi}_0 \hat{F}_r \hat{\chi}_0. \quad (\text{D20})$$

With this preliminary, we will explain the details of the approximation in the simplified parquet method. First, we use the bare vertices  $U_r$  as the fully irreducible vertices  $\Lambda_r$ :

$$\Lambda_c(D) = (U_{\sigma\sigma\sigma\sigma} + U_{\sigma\sigma\bar{\sigma}\bar{\sigma}})(D) = U_c(D), \quad (\text{D21})$$

$$\Lambda_s(D) = (U_{\sigma\sigma\sigma\sigma} - U_{\sigma\sigma\bar{\sigma}\bar{\sigma}})(D) = -U_s(D), \quad (\text{D22})$$

$$\Lambda_e(D) = \frac{1}{2}(U_{\sigma\bar{\sigma}\sigma\bar{\sigma}}^{\text{pp}} - U_{\sigma\bar{\sigma}\bar{\sigma}\sigma}^{\text{pp}})(D) = \frac{1}{4}(U_c + 3U_s)(P), \quad (\text{D23})$$

$$\Lambda_o(D) = \frac{1}{2}(U_{\sigma\bar{\sigma}\bar{\sigma}\sigma}^{\text{pp}} + U_{\sigma\bar{\sigma}\sigma\bar{\sigma}}^{\text{pp}})(D) = -\frac{1}{4}(U_c - U_s)(P). \quad (\text{D24})$$

We calculate susceptibilities by using the random phase approximation (RPA) type formula

$$\hat{\chi}_r(q) = \hat{\chi}_0(q)[\hat{I} + \hat{\Lambda}_r \hat{\chi}_0(q)]^{-1}, \quad (\text{D25})$$

where

$$\hat{\Lambda}_r = z_r \hat{\Lambda}_r, \quad (\text{D26})$$

and  $z_r$  is the constant renormalization factor. With these, the irreducible vertices can be calculated as

$$\hat{\Phi}_r = -\hat{\Lambda}_r \hat{\chi}_r \hat{\Lambda}_r. \quad (\text{D27})$$

By this approximation, the generalized momentum dependences in Eqs. (D1) to (D4) are replaced as

$$D : (k, k', q) \rightarrow q, \quad (\text{D28})$$

$$C : (k, k + q, k' - k) \rightarrow k' - k, \quad (\text{D29})$$

$$P : (k, k', -q - k - k') \rightarrow -q - k - k', \quad (\text{D30})$$

$$X : (k, -k - q, k' - k) \rightarrow k' - k. \quad (\text{D31})$$

If we consider the local case, Eqs. (D28) to (D31) mean that the full vertex has only the diagonal structure.

From the comparison between susceptibilities from the RPA type Eq. (D25) and the parquet type Eq. (D20), we can obtain the renormalization factor  $z_r$  as

$$z_r = 1 + \frac{\text{Tr}[\hat{\chi}_0(k, q)(\hat{\gamma}_r^{(1)}(k - k') + \hat{\gamma}_r^{(2)}(k + k' + q))\hat{\chi}_0(k', q)]}{\text{Tr}[\hat{\chi}_0(q)\hat{\Lambda}_r \hat{\chi}_0(q)]}, \quad (\text{D32})$$

where  $\text{Tr}A = \sum_{k, k', q} \sum_{\alpha} A_{\alpha\alpha\alpha\alpha}(k, k', q)$ . Although the summation in the numerator of Eq. (D32) is taken over  $k, k', q$ , we can rewrite it as a summation over  $q$  by a variable conversion.

Hence, we treat only  $q$  practically. The calculation procedure of the simplified parquet method is as follows.

- (1) Calculate the bare vertices  $\Lambda_r$  by Eqs. (D21) to (D24).
- (2) Calculate the renormalized vertices  $\tilde{\Lambda}_r$  by Eq. (D26). The initial values are  $(z_c, z_s, z_e, z_o) = (1, 0.1, 1, 1)$ .
- (3) Calculate the susceptibilities  $\chi_r$  by Eq. (D25).
- (4) Calculate the reducible vertices  $\Phi_r$  by Eq. (D27).
- (5) Calculate the vertices  $\gamma_r^{(1)}$  and  $\gamma_r^{(2)}$  by Eqs. (D10) to (D17).
- (6) Update the renormalization factor  $z_r$  by Eq. (D32).
- (7) Go back to step 2 (until convergence).

After convergence, we already obtained the vertices  $\Phi_r, F_r$ , and the susceptibilities  $\chi_r$ .

If we obtain the full vertex by the above procedure, we can obtain the self-energy as follows:

$$\begin{aligned} \Sigma_{\alpha\beta}(k) &= \frac{1}{4} \sum_{\gamma\lambda} \sum_q [\hat{F}_c(q) \hat{\chi}_0(q) \hat{U}_c + 3\hat{F}_s(q) \hat{\chi}_0(q) \hat{U}_s]_{\alpha\gamma\beta\lambda} \\ &\times G_{\gamma\lambda}(k+q). \end{aligned} \quad (\text{D33})$$

In practical calculation, however, we omit the contribution from the pp channel in self-energy since it tends to be overestimated.

#### APPENDIX E: CONDITIONS OF THE MODIFIED PARAMETERS IN THE ELECTRON-HOLE SYMMETRIC CASE

Here, we show the conditions which the modified parameters  $A, B$  need to satisfy in the electron-hole sym-

metric case. For simplicity, we consider the single-orbital case.

The spectral representation of the Matsubara self-energy is expressed as

$$\Sigma(\omega_n) = \frac{1}{\pi} \int_{-\infty}^{\infty} d\omega \frac{[-\text{Im}\Sigma(\omega)]}{i\omega_n - \omega}. \quad (\text{E1})$$

Hence, the real part of the Matsubara self-energy is

$$\text{Re}\Sigma(i\omega_n) = \frac{1}{\pi} \int_{-\infty}^{\infty} d\omega \frac{\omega}{\omega_n^2 + \omega^2} \text{Im}\Sigma(\omega). \quad (\text{E2})$$

In the presence of the electron-hole symmetry,  $\text{Im}\Sigma(\omega)$  is an even function, so  $\text{Re}\Sigma(i\omega_n) = 0$ .

On the other hand, the ansatz of the modified-IPT self-energy is

$$\frac{A\Sigma^{2\text{nd}}(i\omega_n)}{1 - B\Sigma^{2\text{nd}}(i\omega_n)}, \quad (\text{E3})$$

where  $\Sigma^{2\text{nd}}(i\omega_n)$  is the second-order self-energy. In the presence of the electron-hole symmetry, the condition which  $A$  and  $B$  need to satisfy is

$$A, iB \in \mathbb{R} \quad (\text{E4})$$

since  $\Sigma^{2\text{nd}}(i\omega_n)$  is a pure imaginary function. When  $B$  is a real number,  $B$  needs to be zero.

- 
- [1] A. Georges, G. Kotliar, W. Krauth, and M. J. Rozenberg, *Rev. Mod. Phys.* **68**, 13 (1996).
- [2] T. A. Maier, M. Jarrell, T. Pruschke, and M. Hettler, *Rev. Mod. Phys.* **77**, 1027 (2005).
- [3] G. Rohringer, H. Hafermann, A. Toschi, A. A. Katanin, A. E. Antipov, M. I. Katsnelson, A. I. Lichtenstein, A. N. Rubtsov, and K. Held, *Rev. Mod. Phys.* **90**, 025003 (2018).
- [4] P. Werner, A. Comanac, L. de' Medici, M. Troyer, and A. J. Millis, *Phys. Rev. Lett.* **97**, 076405 (2006).
- [5] E. Gull, P. Werner, A. Millis, and M. Troyer, *Phys. Rev. B* **76**, 235123 (2007).
- [6] P. Werner and A. J. Millis, *Phys. Rev. B* **74**, 155107 (2006).
- [7] J. Otsuki, H. Kusunose, P. Werner, and Y. Kuramoto, *J. Phys. Soc. Jpn.* **76**, 114707 (2007).
- [8] A. N. Rubtsov, V. V. Savkin, and A. I. Lichtenstein, *Phys. Rev. B* **72**, 035122 (2005).
- [9] A. N. Rubtsov and A. I. Lichtenstein, *J. Exp. Theor. Phys. Lett.* **80**, 61 (2004).
- [10] Y. Nomura, S. Sakai, and R. Arita, *Phys. Rev. B* **89**, 195146 (2014).
- [11] M. Caffarel and W. Krauth, *Phys. Rev. Lett.* **72**, 1545 (1994).
- [12] D. Zgid, E. Gull, and G. K.-L. Chan, *Phys. Rev. B* **86**, 165128 (2012).
- [13] H. Ishida and A. Liebsch, *Phys. Rev. B* **81**, 054513 (2010).
- [14] A. Liebsch, *Phys. Rev. B* **84**, 180505(R) (2011).
- [15] A. Liebsch and H. Ishida, *J. Phys.: Condens. Matter* **24**, 053201 (2011).
- [16] K. Yosida and K. Yamada, *Prog. Theor. Phys. Suppl.* **46**, 244 (1970).
- [17] K. Yamada, *Prog. Theor. Phys.* **53**, 970 (1975).
- [18] K. Yosida and K. Yamada, *Prog. Theor. Phys.* **53**, 1286 (1975).
- [19] K. Yamada, *Prog. Theor. Phys.* **54**, 316 (1975).
- [20] A. Georges and G. Kotliar, *Phys. Rev. B* **45**, 6479 (1992).
- [21] H. Kajueter and G. Kotliar, *Phys. Rev. Lett.* **77**, 131 (1996).
- [22] M. Potthoff, T. Wegner, and W. Nolting, *Phys. Rev. B* **55**, 16132 (1997).
- [23] L.-F. Arsenault, P. Sémon, and A.-M. S. Tremblay, *Phys. Rev. B* **86**, 085133 (2012).
- [24] T. Saso, *J. Phys.: Condens. Matter* **13**, L141 (2001).
- [25] T. Fujiwara, S. Yamamoto, and Y. Ishii, *J. Phys. Soc. Jpn.* **72**, 777 (2003).
- [26] M. S. Laad, L. Craco, and E. Müller-Hartmann, *Phys. Rev. Lett.* **91**, 156402 (2003).
- [27] N. Dasari, W. R. Mondal, P. Zhang, J. Moreno, M. Jarrell, and N. S. Vidhyadhiraja, *Eur. Phys. J. B* **89**, 202 (2016).
- [28] Y. A. Bychkov, L. P. Gor'kov, and I. E. Dzyaloshinski, *J. Exp. Theor. Phys.* **50**, 738 (1966).
- [29] G. Rohringer, A. Valli, and A. Toschi, *Phys. Rev. B* **86**, 125114 (2012).
- [30] V. Janiš, *J. Phys.: Condens. Matter* **10**, 2915 (1998).
- [31] V. Janiš, *Phys. Rev. B* **60**, 11345 (1999).

- [32] H. Kusunose, *J. Phys. Soc. Jpn.* **79**, 094707 (2010).
- [33] V. Janiš and P. Augustinský, *Phys. Rev. B* **75**, 165108 (2007).
- [34] P. Augustinský and V. Janiš, *Phys. Rev. B* **83**, 035114 (2011).
- [35] T. Schäfer, S. Ciuchi, M. Wallerberger, P. Thunström, O. Gunnarsson, G. Sangiovanni, G. Rohringer, and A. Toschi, *Phys. Rev. B* **94**, 235108 (2016).
- [36] J. Kaufmann, P. Gunacker, and K. Held, *Phys. Rev. B* **96**, 035114 (2017).
- [37] A. Tagliavini, S. Hummel, N. Wentzell, S. Andergassen, A. Toschi, and G. Rohringer, *Phys. Rev. B* **97**, 235140 (2018).
- [38] J. Kaufmann, P. Gunacker, A. Kowalski, G. Sangiovanni, and K. Held, *Phys. Rev. B* **100**, 075119 (2019).
- [39] N. Wentzell, G. Li, A. Tagliavini, C. Taranto, G. Rohringer, K. Held, A. Toschi, and S. Andergassen, *Phys. Rev. B* **102**, 085106 (2020).
- [40] N. E. Bickers, D. J. Scalapino, and S. R. White, *Phys. Rev. Lett.* **62**, 961 (1989).
- [41] R. Mizuno, M. Ochi, and K. Kuroki (unpublished).
- [42] P. Seth, I. Krivenko, M. Ferrero, and O. Parcollet, *Comput. Phys. Commun.* **200**, 274 (2016).
- [43] E. Gull, Ph.D. thesis, ETH Zürich, 2008.
- [44] L. V. Boehnke, Susceptibilities in materials with multiple strongly correlated orbitals, Ph.D. thesis, Universität Hamburg, 2015.
- [45] L. Boehnke, H. Hafermann, M. Ferrero, F. Lechermann, and O. Parcollet, *Phys. Rev. B* **84**, 075145 (2011).
- [46] O. Parcollet, M. Ferrero, T. Ayrál, H. Hafermann, I. Krivenko, L. Messio, and P. Seth, *Comput. Phys. Commun.* **196**, 398 (2015).
- [47] R. Arita and K. Held, *Phys. Rev. B* **72**, 201102(R) (2005).
- [48] This is qualitatively consistent with the results of the two-orbital Bethe lattice with crystal field splitting shown in Sec. 3.5 in Ref. [27]. The situation studied in Sec. 3.5 in Ref. [27] is even further away from half-filling than  $n = 1.3$  studied here. ( $n_{\text{tot}} = 1.1$  in Ref. [27] corresponds to  $n = 0.55$  in our study, and by electron-hole transformation, this corresponds to  $n = 1.45$  in our case). The deviations of the MO-IPT results from that of CT-QMC are larger than that in Ref. [27] since the DOS of the two-dimensional square lattice exhibits a van Hove singularity (in contrast to the Bethe lattice adopted in Ref. [27]), so that the quasiparticle weight is sensitive to the on-site energy difference. These results suggest that caution has to be taken when we apply the MO-IPT to systems with on-site energy difference.
- [49] D. Bergeron and A.-M. S. Tremblay, *Phys. Rev. E* **94**, 023303 (2016).
- [50] H. Kusunose, *J. Phys. Soc. Jpn.* **75**, 054713 (2006).
- [51] (core hours) = (the number of CPU cores we use)  $\times$  (the number of hours for a calculation).
- [52] S. Koley, M. S. Laad, N. S. Vidhyadhiraja, and A. Taraphder, *Phys. Rev. B* **90**, 115146 (2014).
- [53] S. Koley, M. S. Laad, and A. Taraphder, *Sci. Rep.* **7**, 10993 (2017).
- [54] L. Craco and S. Leoni, *Phys. Rev. B* **100**, 121101(R) (2019).
- [55] M. S. Laad, L. Craco, and E. Müller-Hartmann, *Phys. Rev. B* **73**, 045109 (2006).
- [56] L. Craco, *Phys. Rev. B* **96**, 165412 (2017).
- [57] L. Craco and S. Leoni, *Phys. Rev. B* **100**, 115156 (2019).
- [58] Dasari *et al.* also studied an orbital nondegenerate system in Ref. [27], where MO-IPT shows good agreement with CT-QMC for cases away from half-filling.
- [59] Y. Kuramoto, *Z. Phys. B* **53**, 37 (1983).
- [60] R. Bulla, T. A. Costi, and T. Pruschke, *Rev. Mod. Phys.* **80**, 395 (2008).